Naval Research Laboratory

Washington, DC 20375-5320

AD-A279 716

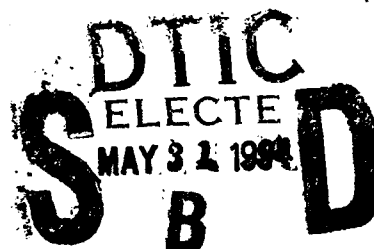# PRS Scoping Study I: Scaling Law Estimates for K-Shell Radiation Yields on JUPITER-Class Generators

J. L. Giuliani, Jr.
J. Davis
M. Mulbrandon
K. Whitney
J. W. Thornhill

Radiation Hydrodynamic Branch
Plasmas Physics Division

DTIC
ELECTE
MAY 3 1 1994
B

May 31, 1994

94-16081

94 5 27 035

DTIC QUALITY INSPECTED 1

REPORT DOCUMENTATION PAGE

Form Approved
OMB No. 0704-0188

1. AGENCY USE ONLY (Leave Blank)	2. REPORT DATE May 31, 1994	3. REPORT TYPE AND DATES COVERED

4. TITLE AND SUBTITLE
PRS Scoping Study I: Scaling Law Estimates for K-Shell Radiation Yields on JUPITER-Class Generators

5. FUNDING NUMBERS

6. AUTHOR(S)
J. L. Giuliani, Jr., J. Davis, M. Mulbrandon, K. Whitney, and J. W. Thornhill

7. PERFORMING ORGANIZATION NAME(S) AND ADDRESS(ES)
Naval Research Laboratory
Washington, DC 20375-5320

8. PERFORMING ORGANIZATION REPORT NUMBER

NRL/MR/6720--94-7466

9. SPONSORING/MONITORING AGENCY NAME(S) AND ADDRESS(ES)
Defense Nuclear Agency
RAEV
Alexandria, VA 22310

10. SPONSORING/MONITORING AGENCY REPORT NUMBER

11. SUPPLEMENTARY NOTES

12a. DISTRIBUTION/AVAILABILITY STATEMENT
Approved for public release; distribution unlimited.

12b. DISTRIBUTION CODE

13. ABSTRACT (Maximum 200 words)

The radiation output from krypton, argon, and xenon z-pinch loads are calculated for JUPITER-class generators using an amended version of the Whitney, et al., K-shell yield scaling law. The present version, termed J-scaling law, is directed toward JUPITER predictions and includes a dependence on the final radius as well as a smooth yield fall off for weak implosions. When combined with a circuit model and a thin shell model for the plasma pinch dynamics, comparisons and predictions of yields can be made for specific machines. Comparisons with existing aluminum data on DOUBLE EAGLE and SATURN demonstrate the veracity of the J-scaling law. A simple equivalent circuit with variable driving voltage is used to predict the trend of K-shell yield with increasing load current. In general, for JUPITER-class machines (30 — 100 MA) Ar is in the efficient I^2 scaling regime, xenon is in the weak I^4 regime, and Kr is a transition radiator. Candidate transmission line circuits for the Linear Inductive Adder (LIA) and the modular Inductive Energy Store (IES) JUPITER designs are investigated in detail. Load currents, voltages, and coupled kinetic energies are calculated as a function of MR_0^2. These calculations are then combined with the J-scaling law to predict K-shell yields for the transmission line circuits. Variations of the standard candidate point designs are also investigated: specifically, the effects of a larger front end inductance, of eliminating a closing switch in the LIA, and of increasing the conduction time on the IES.

The results include the following: the standard design of each candidate machine produces similar peak K-shell yields for Ar ($\sim$7 MJ), Kr ($\sim$3 MJ), and Xe ($\sim$0.3 MJ). For a fixed pinch length, the LIA can achieve near peak performance with smaller initial radii than the IES. This difference would be important if Rayleigh-Taylor instabilities are found to significantly reduce the yields from large diameter loads. The yields from low Z elements, such as Ar, are optimized with long ($\sim$6 cm) pinches, while short ($\sim$2 cm) pinches optimize high Z-element (e.g., Xe) yields. Increasing the front end inductance is detrimental to the IES but not the LIA. Finally, employing a long conduction switch on the IES can lead to significantly enhanced yields, but only if $\sim$10 MV can be withstood across the switch and the switch opening is not degraded below that of the standard design. The above investigations using a scaling law rely on and are limited by certain assumptions about the stagnation physics, ionization dynamics, and load stabilization. These limitations are discussed in light of recommendations for future theoretical research on JUPITER plasma loads.

14. SUBJECT TERMS

15. NUMBER OF PAGES
69

16. PRICE CODE

17. SECURITY CLASSIFICATION OF REPORT UNCLASSIFIED	18. SECURITY CLASSIFICATION OF THIS PAGE UNCLASSIFIED	19. SECURITY CLASSIFICATION OF ABSTRACT UNCLASSIFIED	20. LIMITATION OF ABSTRACT UL

CONTENTS

PRS SCOPING STUDY I: SCALING LAW ESTIMATES FOR K-SHELL RADIATION YIELDS ON JUPITER-CLASS GENERATORS

I. Introduction

For over a decade the Defense Nuclear Agency has supported pulsed power generator development as a power source for certain aspects of above ground radiation effects testing. Generators such as BLACKJACK 5, DOUBLE EAGLE, SATURN, and PHOENIX transfer energy initially stored in a Marx bank through a water line to a front end. For cool and warm photon production (0 – 15 keV) the front end of the machine incorporates a z-pinch load. In a z pinch the plasma formed out of a wire array or gas puff is accelerated inward by the surrounding magnetic pressure arising from the axial current and produces a plasma radiation source (PRS) at implosion. SATURN, the largest working generator, develops up to ~10 MA of load current, implodes the plasma with ~200 kJ of kinetic energy, and produces ~75 kJ of aluminum K-shell emission. This emission primarily consists of radiation above 1.6 keV from bound-bound and free-bound atomic transitions of hydrogen- and helium-like ionization stages of aluminum. Although the DECADE generator under construction will reach 15 – 20 MA peak load current and deliver almost 1.5 MJ of plasma kinetic energy, this is probably insufficient to strongly ignite K-shell krypton with emission in the > 13 keV range. With the cessation of underground testing the goal of the next generation of pulse power drivers is to produce mega-joules of radiation in the 0 – 15 keV range, and several hundred kilo-joules at 30 keV. To achieve this, far larger currents and kinetic energies are needed to heat plasma with atomic numbers $\gtrsim 36$ into their K-shell stage. Concept studies are under way for the JUPITER generator which is envisioned to reach ~60 MA and deliver ~15 MJ of kinetic energy. At present it is unclear whether these ambitious current and kinetic energy objectives will convert into the radiation yields required to meet the projected test requirements. Hence a scoping study for PRS yields on JUPITER-class generators has been undertaken within the Plasma Physics Division at the Naval Research Laboratory. This paper is one of several reporting on the scoping study for estimated radiation yields. Since the current and energy parameters of JUPITER will be so much larger than present day machines, the scoping study is necessarily an extrapolation of theoretical and computer simulation analyses which have been benchmarked to existing machines.

In the present paper we employ a K-shell radiation scaling law to predict radiation yields from JUPITER-class generators. Scaling laws offer the utility of surveying large regions of load and driver parameter space within a short time. The particular scaling law we use has a long history of development and continues to do so even in this paper. Essential elements of the scaling formulas in regard to the dependence on the atomic number Z were brought forth in the initial paper by Apruzese and Davis [Ref.1]. Later, detailed work involving theory and computer simulations by Whitney, et al., [Ref.2] substantially altered the approach into a kinetic energy scaling law. Subsequent improvements to match the soft implosions observed in experiments were recently

reported by Thornhill, et al., [Ref.3]. The accuracy of this scaling law for low Z material like aluminum is analogous to being substantially "in the ballpark," as shown in Whitney, et al., [Ref.4]. However, to apply the existing scaling law to JUPITER requires modifications in order to (i) treat large initial radii (≥ 4 cm) implosions and (ii) account for kinetic energies which are just able to thermalize high Z (≥ 36) plasmas into the K-shell ionization stage. Neither of these conditions were within the purview of the original law. The revised scaling law is developed in Section II, and hereinafter will be referred to as the revised or J-scaling law ("J" for JUPITER). As the accuracy of this revised law is less well determined than the original one, comparisons with aluminum data from DOUBLE EAGLE and SATURN in Section III will clarify its viability for weak implosions, *ala* case (ii) above. In Section IV an open circuit voltage waveform appropriate to a JUPITER-class machine is adopted to drive a simple equivalent circuit. The magnitude of the driving voltage is scaled so that the peak load current ranges from 10 to 100 MA. The dependence of the K-shell radiation from aluminum (>1.6 keV), argon (>3.1 keV), krypton (>13 keV), and xenon ($\gtrsim 28$ keV) pinches over this range of currents is investigated with the J-scaling law. Following this, two specific design options for JUPITER are evaluated in Section V: (i) an Inductive Energy Store (IES) design with a Plasma Opening Switch (POS) in each module, and (ii) a modular Linear Inductive voltage Adder (LIA). Since the Jupiter Design Option Study Team (JDOST) began in the summer of 1993, there has been a significant downselection in the machine options and changes in the modular IES and LIA designs. Section V is restricted to the standard designs as of the fourth JDOST meeting in January, 1994. In Section VI several important variations of the standard point designs derived from the inherent flexibility of the circuits are considered for optimizing the yields.

As this is a rather lengthy report the last section (VII) contains a summary of the results and conclusions obtained during this study with the revised J-scaling law. Among these results are several primary findings. (i) The maximum K-shell radiation yields Y_K for the standard designs of the LIA and IES options are fairly similar: $Y_K(\text{Ar}) \sim 7$ MJ; $Y_K(\text{Kr}) \sim 3$ MJ; and $Y_K(\text{Xe}) \sim 0.3$ MJ. This is not coincidental; the JDOST process itself has driven the standard designs toward similar capabilities through the process of competition. (ii) One significant difference between the designs is the peak yield variation with initial radius R_0 at a fixed pinch length: the LIA is predicted to approach its maximum radiation yield at smaller initial radii than the IES. This differences arises from the shorter voltage pulse on the LIA relative to the IES and may turn out to be relevant in limiting the possible disruption caused by the Rayleigh-Taylor instability during the run-in phase [Ref.5]. On the other hand, Davis [Ref.6] has shown that alternative load configurations may mitigate the deleterious effects of such instabilities, so the advantage of small R_0 needs further investigation. (iii) The yield from low atomic number (Z) material, such as argon, is optimized with long pinch lengths (~ 6 cm), while the opposite is true for high Z elements, such as xenon.

Because argon is in the efficient scaling regime for JUPITER, its yield varies directly with the total kinetic energy, which is maximized in long pinches. Xenon, however, is in the extremely inefficient I^4 regime where the yield depends more on the kinetic energy per unit length. (iv) A factor of two increase to the front end inductance does not alter the peak K-shell yields on the LIA design, but reduces those for the IES by $\sim 2/3$. If the presently designed convolute is eventually found to be insufficient in maintaining vacuum insulation one may be forced to opt for a higher inductance front end. (v) If the POS on the IES can attain long conduction times then the radiation yields from the IES are significantly greater than those from the LIA. This advantage can be realized only if the POS can open in the same manner as the shorter conduction, standard IES design while sustaining ~ 10 MV.

The yield comparisons between the IES and LIA design options are subject to many caveats: Radiation yield scaling laws may not extrapolate from aluminum on present day generators up to krypton, and especially xenon, on JUPITER; the stagnation physics of the pinch at ~ 60 MA may be fundamentally different than at ≤ 10 MA; the ionization dynamics for the high Z elements is much more dependent on the L- and M-shell radiation, because it is so energetic, than low Z elements (such as aluminum) are dependent on their UV L-shell radiation; and uncontrolled or poorly understood instabilities may reduce the projected yields found at large radii in the present study. The last section also discusses these limitations and concomitant future research directions for JUPITER load analysis.

II. Revised K-Shell Yield J-Scaling Law

The K-shell yield J-scaling relation is based on that given by Whitney, et al. [Ref.1], and Thornhill, et al. [Ref.2], with two revisions: (i) a final radius dependency in the inefficient regime, and (ii) a yield reduction factor to account for energetically weak implosions. Let us begin by first defining a parameter η, as presented in the above cited papers, which measures the kinetic energy per atom in an imploding plasma in terms of a minimum energy:

$$\eta \equiv \frac{\frac{1}{2} m_i v_{imp}^2}{E_{min}}. \tag{1}$$

Here m_i is the atomic mass of the element under consideration, v_{imp} is the final maximum implosion velocity, and E_{min} is the minimum energy needed to reach and maintain an individual atom of the element under consideration in the K-shell. Specifically, E_{min} is the sum of the ionization energies required to strip the atom to a 50% helium-like and 50% hydrogen-like configuration

3

plus the thermal energy of a hydrogen-like ion at a temperature for which K-shell occupation and excitation is strong. Equations (33) and (46) of Ref.1 provide simple relations for m_i and E_{min} in terms of the atomic number Z:

$$m_i \approx 1.58 Z^{1.1} m_p \qquad \text{and} \qquad E_{min} \approx 1.49 Z^{3.51} \quad \text{eV/ion}, \qquad (2)$$

where m_p is the proton mass. Hence from eqns.(1) and (2), $\eta \approx 0.55[v_{imp}/(cm/\mu s)]^2 Z^{-2.41}$.

The K-shell yield per unit length, including the revisions of the present paper, is written as

$$\left(\frac{Y_K/\ell}{kJ/cm}\right) = \text{smaller of} \begin{cases} 10^6 \epsilon_L(\eta)\left(\frac{0.5mm}{R_f}\right) a_o(\eta) a_Z(Z)\left(\frac{M/\ell}{mg/cm}\right)^2, & (3a) \\[2mm] 10^{-1} \epsilon_L(\eta)\epsilon_K \frac{1}{2}\left(\frac{v_{imp}}{cm/\mu s}\right)^2 \left(\frac{M/\ell}{mg/cm}\right), & (3b) \end{cases}$$

where M is the total mass loading, ℓ is the pinch length, and R_f is the final implosion or stagnation radius where the plasma reaches the velocity v_{imp}.

From eqns.(39), (42), and (43) of Ref.1 the coefficients $a_o(\eta)$, $a_Z(Z)$, and ϵ_K are

$$a_o(\eta) = 33.7 + \frac{595}{\eta} - \frac{70.7}{\eta^2} \quad (kJ\,cm/mg^2),$$

$$a_Z(Z) = \frac{\exp(-20.6/Z^{0.9})}{Z^{3.55}}, \qquad (4)$$

$$\epsilon_K = 0.3.$$

The function $a_o(\eta)$ is based on 1-D multi-zone numerical simulations for high η implosions with aluminum. These radiation-magnetohydrodynamic calculations employ a linear rising current ramp until the outer radius of the plasma reaches 0.14 cm, after which the current is turned off in order that the K-shell yield reflect only the kinetic energy input. The current cutoff radius is larger than the final compression radius of the pinch. ϵ_K is also determined form these simulations and represents the conversion efficiency of total kinetic energy into K-shell radiation. The actual calculations display a range for ϵ_K from 0.25 to 0.5, but for the present discussion we will fix it at a conservative value of 0.3. The formula for $a_Z(Z)$ is based upon Z-scaling of the He-α line radiation in the coronal approximation.

The two remaining factors in eqn.(3), namely R_f and $\epsilon_L(\eta)$, arise from the present revisions. The form of the R_f dependence in eqn.(3a) derives from the formula for optically thin emission lines as found in eqn.(41) of Ref.1. Though Whitney, et al. did not include any radius dependence, it is important to do so for a JUPITER study. Proposed circuit designs require large initial radii (R_o) in order to realize peak performance. The final radius for $R_o > 2$ cm may be significantly larger

than the 1 – 3 mm typically seen on DOUBLE EAGLE and SATURN. Thornhill, et al. [Ref.2] determined that soft implosions on machines like DOUBLE EAGLE and SATURN may reflect an enhancement of the transport coefficients. For soft, i.e., weak compression, implosions the yield in the inefficient regime of eqn.(3a) is reduced by $1/_6$. In effect, we have replaced this softening with a final radius dependency because enhanced turbulent transport in the pinch translates into an increased stagnation radius at implosion. The scale factor for the radius dependence in eqn.(3a), namely 0.5 mm, was determined by matching the $1/_6$ reduction factor with a typical final radius seen on existing experiments.

The second revision, $\epsilon_L(\eta)$, concerns a reduction of the K-shell yield for implosions with η near unity. The original scaling law of Whitney, et al., was not meant to apply to such energetically weak and poorly ionized implosions, but for krypton and xenon on JUPITER it will be shown that the implosions with the highest yields are in this regime. Clearly, there will be no K-shell yield for $\eta = 0$, while for $\eta \gg 1$ one should join smoothly with the relations of eqn.(3). For simplicity we assume that ϵ_L varies linearly with η in the region of $\eta \sim 1$ and find a fit to calculated krypton K-shell yields from a JUPITER prototype design. We performed a total of 96, multi-zone, radiation-magnetohydrodynamic simulation runs with peak load currents ranging from 30 to 80 MA and η ranging from 0.5 to 3. The comparison between numerical simulations and the J-scaling relation is presented in Fig.1. The resultant form for the low η correction of eqn.(3) is given by

$$\epsilon_L(\eta) = \begin{cases} 1, & \text{for } \eta \geq 3; \\ \dfrac{2\eta - 1}{5}, & \text{for } 0.5 \leq \eta \leq 3; \\ 0, & \text{for } \eta \leq 0.5. \end{cases} \tag{5}$$

The complete K-shell radiation J-scaling law of eqns.(3), (4), and (5) is now seen to be dependent upon five parameters:

$$Y_K = Y_K(Z, R_f, \ell, v_{imp}, M). \tag{6}$$

For a chosen material (Z) and final radius (R_f), the K-shell yield (Y_K) per unit length (ℓ) can be calculated as a function of the velocity (v_{imp}) and mass loading (M) per unit length. The yield thus depends solely upon the plasma conditions at implosion. Figure 2a presents contours of aluminum K-shell yield per unit length (Y_K/ℓ) displayed over the $v_{imp} - M/\ell$ plane with R_f fixed at 0.1 cm. Several horizontal η markers are shown at the right hand side and the mass breakpoint curve is noted as a dotted line. The breakpoint mass $(M/\ell)_{BP}$ is determined by equality between the relations in eqn.(3):

$$\left(\frac{M/\ell}{\text{mg/cm}}\right)_{BP} = 10^{-7}\frac{1}{2}\epsilon_K\left(\frac{v_{imp}}{\text{cm}/\mu\text{s}}\right)^2\frac{(R_f/0.5\text{mm})}{a_o(\eta)a_Z(Z)}. \tag{7}$$

5

For $M/\ell < (M/\ell)_{BP}$ one is in the inefficient regime and the yield scales as M^2 as in eqn.(3a). This is equivalent to the so called "I^4" current scaling regime. Otherwise, one is in the efficient regime where the yield varies as M/ℓ and scales linearly with the total kinetic energy ($\propto I^2$) of the implosion.

Consider a line of constant final kinetic energy per unit length, E_K/ℓ, in Fig.2a running from the lower right to the upper left. Starting from the large mass, low velocity regime, the yield increases as one moves upward from $\eta = 0.5$ toward the $\eta = 3$ level. This increase reflects the gradual turning on of the K-shell emitters as the mass is decreased and the velocity increased. The functional form of ϵ_L is important over this part of the graph. Between the $\eta = 3$ line and the M_{BP}/ℓ curve, the Y_K/ℓ contours are straight lines parallel to constant kinetic energy levels. This is the efficient regime where Y_K scales linearly with E_K. Moving above the M_{BP}/ℓ curve toward the upper left, one sees that the yield drops off. Here there is sufficient implosion velocity to thermalize the plasma into or beyond the K-shell ionization stage, but the mass is too small to radiate efficiently. Hence this is the inefficient regime and the yield scales as $(M/\ell)^2$. If a larger R_f is chosen, the M_{BP}/ℓ curve shifts to the right and the efficient regime shrinks in size. For comparison, krypton yield contours over the $v_{imp} - M/\ell$ plane are presented in Fig.2b. Note in this latter figure that lines of constant η have move upward compared to Fig.2a because the velocity needed to thermalize krypton to the K-shell is larger than for aluminum. As a matter of fact, the $\eta = 3$ line is above the M_{BP}/ℓ curve out to the $Y_K/\ell \sim 3$ MJ/cm contour. Thus the efficient regime has nearly disappeared for krypton unless one can drive a mass loading of ~ 10 mg/cm to $\gtrsim 2 \times 10^8$ cm/sec and stagnate at 0.1 cm. As this condition is unlikely to be met by presently envisioned JUPITER pulse power drivers, one can conclude that krypton implosions will be in the $\eta \sim 1$ regime and the K-shell yields will be dependent on the details of the plasma during stagnation. The classical I^4 scaling law relating different generators is reflected in graphs like Fig.2b where the maximum load kinetic energy produced by a machine lies along a line to the left of the efficient regime. Hence no variation of the mass loading in such a case can put one into the efficient scaling regime.
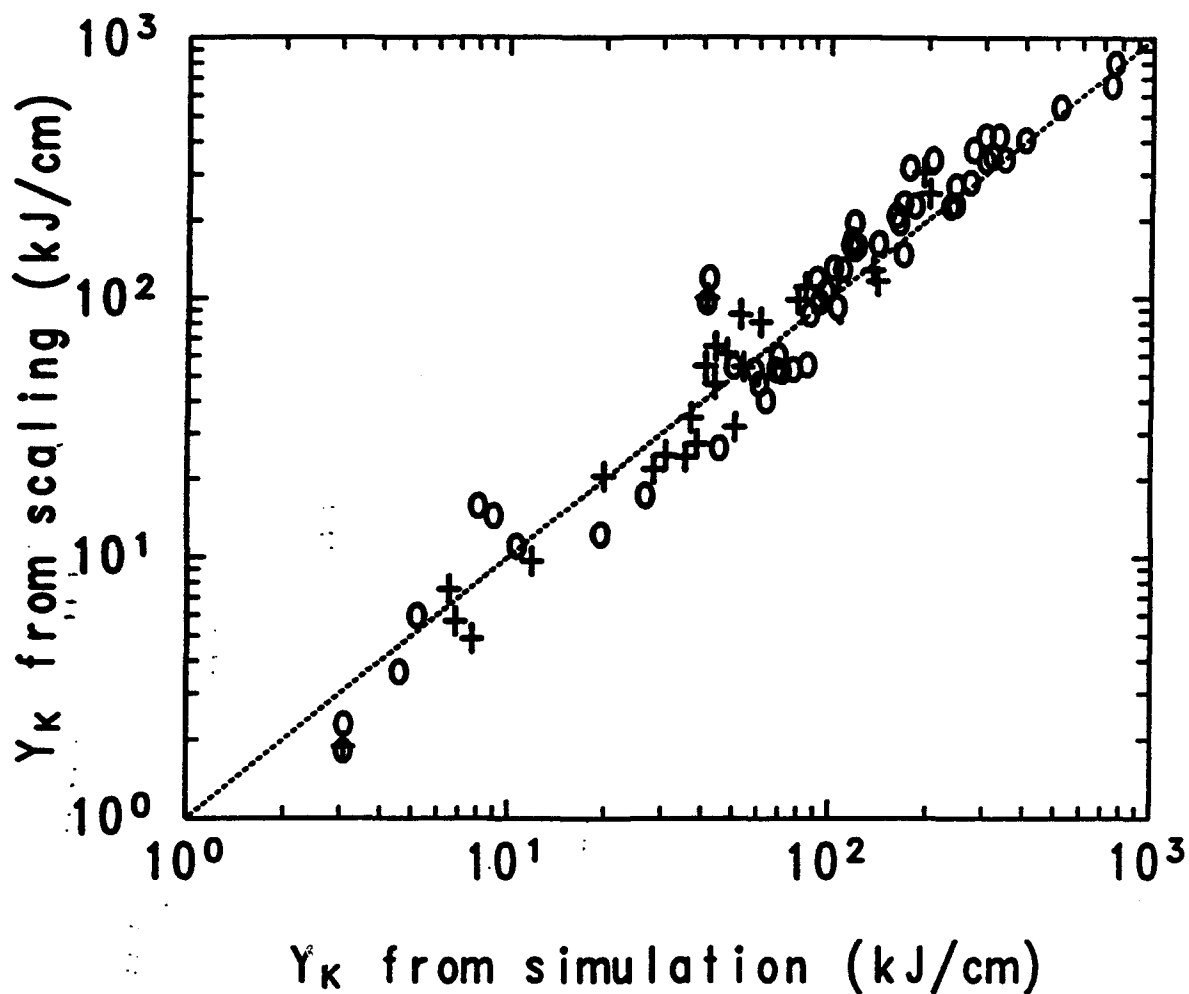
Fig.1 Comparison between krypton K-shell yields from multi-zone, radiation-hydromagnetic simulations on a JUPITER prototype design with the results from the scaling law of eqn.(3). The fit is used to determine the factor ϵ_L in the scaling law for energetically weak ($\eta \sim 1$) implosions.
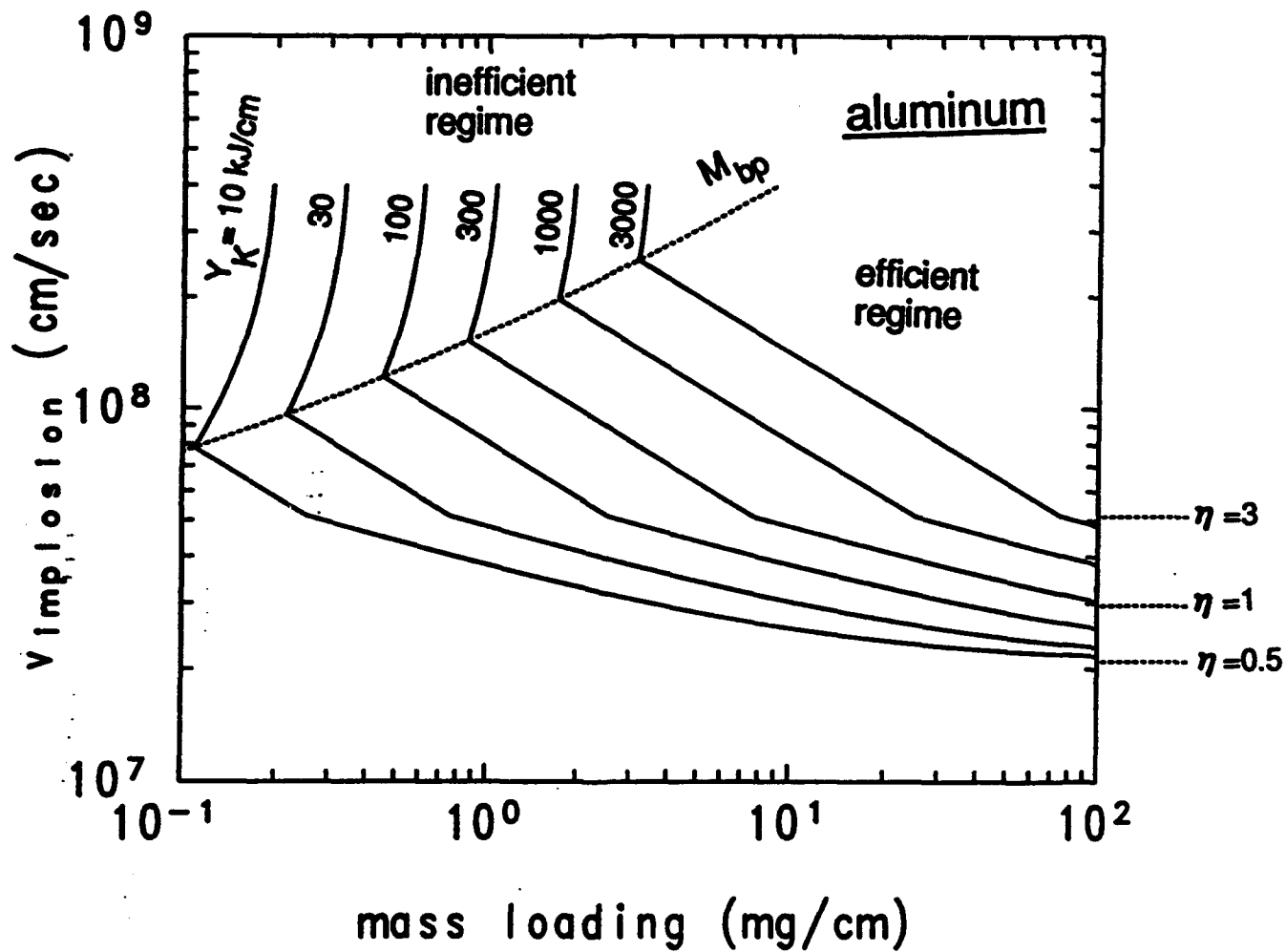
Fig.2(a) Contours of aluminum K-shell yield over the plane of initial mass vs final implosion velocity. The stagnation radius, R_f, is fixed at 0.1 cm. Horizontal lines of constant η are noted on the left and the mass breakpoint curve dividing the efficient (yield $\propto$ mass) from the inefficient (yield $\propto$ mass^2) regimes is dotted. Weak implosions occur for $\eta < 3$.

Fig.2(b) Same as Figure 2a except for krypton. The shift of the curves upward and to the right compared to Figure 2a reflects the difficulty in reaching the K-shell ionization stage of krypton.

III. Comparison of Revised J-Scaling Law with Aluminum Data

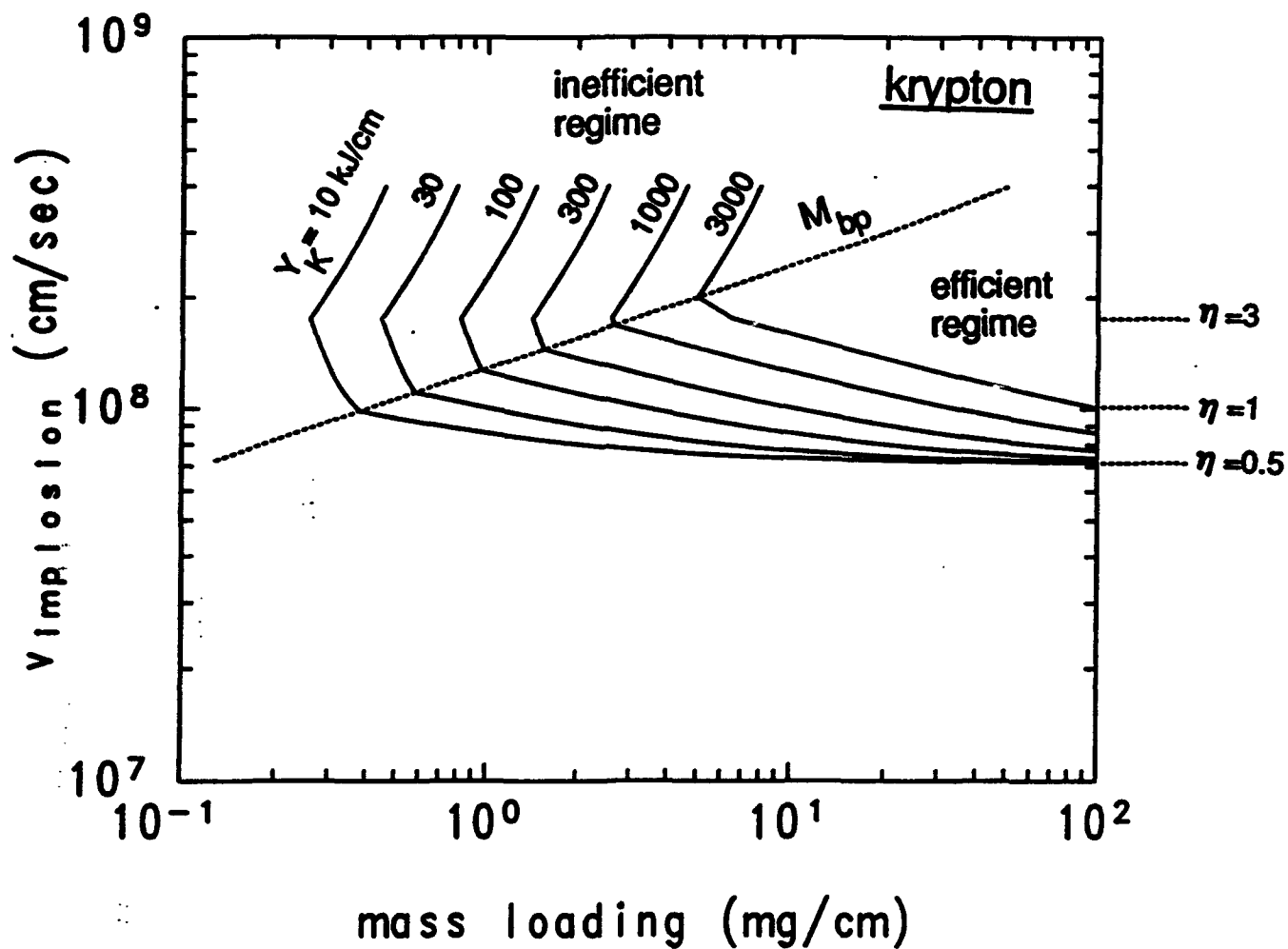The results presented in Figure 2 are independent of the machine in that the kinetic energy at implosion is a free parameter. Let us apply the J-scaling relation to existing machines where the energy coupled to the load is a function of the driver. Such an analysis will display the level of accuracy in the J-scaling law. There has been a substantial number of z-pinch experiments on DOUBLE EAGLE and SATURN wherein K-shell radiation was measured. We concentrate on those experiments which employed aluminum wire-array implosions. Wire arrays offer the advantage of *a priori* knowledge of the initial radius R_o and mass loading M, as opposed to gas puffs where R_o depends on the nozzle tilt angle and the actual M mass can only be estimated from implosion times. One can calculate the K-shell yield by combining the J-scaling law of Section II with a thin shell model for the dynamics of the pinch as driven by a circuit.

The momentum equation for thin shell dynamics is

$$M\frac{dv}{dt} = -2\pi r \ell \frac{B^2}{8\pi} = \frac{\ell}{rc^2}I^2,$$ (8)

where r and v are the instantaneous radius and velocity of the plasma shell, I is the load current, c is the speed of light, and the force acting to implode the plasma is given the magnetic field B pressure at the surface of the plasma. In cgs units with $\mu_o = 4\pi/c^2$, $B = 2I/rc$. The generator is treated as a simple open circuit voltage driver V_{oc} with a machine impedance Z_o and feed inductance L_o:

$$L_o\frac{dI}{dt} + Z_oI = V_{oc} - \frac{d}{dt}\Big[\frac{2\ell}{c^2}\ln(\frac{R_w}{r})I\Big].$$ (9)

Here R_w is the return current radius in the pinch region and and the pinch inductance is contained in the last term. The above equations can be simplified by the transformation to the variables

$$r = xR_o \qquad \text{and} \qquad v = \frac{dx}{dt}R_o = \dot{x}R_o,$$ (10)

where R_o is the initial radius of the plasma shell. One finds for eqn.(8)

$$(MR_o^2)\frac{d\dot{x}}{dt} = -\frac{\ell}{xc^2}I^2,$$ (11)

and then eqn.(9) becomes

$$\Big[L_o + L_w - \frac{2\ell}{c^2}\ln x\Big]\frac{dI}{dt} + \Big[Z_o - \frac{2\ell}{c^2}\frac{\dot{x}}{x}\Big]I = V_{oc}.$$ (12)

10

Here the initial load inductance is given by

$$L_w = \frac{2\ell}{c^2}\ln\left(\frac{R_w}{R_o}\right). \tag{13}$$

As noted by Katzenstein [Ref.7] (see also Mosher [Ref.8]), the coupled circuit-pinch dynamics for the thin shell model depends on the load configuration through the quantities MR_o^2, L_w, and R_f/R_o. Starting from $x = 1$ and $\dot{x} = 0$ at $t = 0$, eqns.(11) and (12) are advanced in time until the plasma shell reaches a normalized stagnation radius $x_f = R_f/R_o$. This instant corresponds to the implosion time t_{imp} with a normalized final velocity $\dot{x}_f = v_{imp}/R_o$. Multiplying eqn.(11) by $\dot{x}$ and integrating in time one finds the kinetic energy E_K of the pinch. Hence for a given machine, $\{L_o, Z_o, V_{oc}(t)\}$, pinch length ℓ, initial inductance L_w, and compression ratio x_f, one has

$$t_{imp}(MR_o^2), \quad \dot{x}_f(MR_o^2), \quad \text{and} \quad \frac{1}{2}Mv_{imp}^2 = E_K(MR_o^2). \tag{14}$$

For DOUBLE EAGLE $L_o = 39$ nH and $Z_o = 0.3\Omega$; for SATURN $L_o = 9.75$ nH and $Z_o = 0.167\Omega$. In the experiments 2 cm long wires were used. The present calculations fix the initial load inductance L_w at 3 nH, independent of R_o, and assume a compression ratio R_f/R_o of $1/7$. The driving voltages V_{oc} for DOUBLE EAGLE and SATURN are displayed in Figs.3a and 4a, respectively.

Given the above information, the calculated current profiles for various MR_o^2 on the two machines follow in Figs.3b and 4b. Note the increased "softness" or inductive notch of the SATURN driver as compared to DOUBLE EAGLE, i.e., the larger turnover in the current profiles as the implosion proceeds. Implosion times t_{imp} can be measured in a similar fashion as done in experiments: The first fiducial time mark is the intercept between a linear fit to the rising load current and the temporal axis, as indicated in Fig.3b and 4b by the dotted lines. The second fiducial time is the endpoint of the current waveform, which occurs when the plasma shell reaches its prespecified compression ratio. The implosion time is the difference between these two noted times. A comparison of the implosion times t_{imp} over MR_o^2 for the two machines is presented in Fig.5a. The compressed voltage pulse of SATURN relative to DOUBLE EAGLE's shows up in its significantly shorter implosion times. The kinetic energy of the plasma at implosion, E_K, is likewise compared in Fig.5b for the two machines. The peak E_K occurs at $MR_o^2 \sim 2$ mg cm^2 for both machines, and, as expected from eqn.(11), the ratio of E_K at this point (250 kJ/ 60 kJ) scales about as the square of the ratio of the peak I_{load}, (10 MA/4.5 MA)^2.

To compute the K-shell yield from the J-scaling law one needs the quantities listed in eqn.(6). For the aluminum experiments, $Z = 13$ and $\ell = 2$ cm. Consider a solution for a some MR_o^2 as given in eqn.(14) and arbitrarily chose an initial radius R_o. Then the total mass M is specified

11

since MR_o^2 is known, the final radius R_f is specified by the assumed compression ratio parameter x_f, and the final dimensional velocity is given through $v_{imp} = R_o \dot{x}_f$. Eqn.(3) can now be used to compute the aluminum K-shell yield estimate for this chosen value of R_o. Varying R_o for the same MR_o^2 will then give a set of yields $Y_K(MR_o^2, R_o)$. Note that each of these yield estimates have the same kinetic energy coupled to the load but, in general, the Y_K vary. Finally repeat the whole procedure for a range of MR_o^2 values. The complete results can be presented as a contour map of the K-shell yield in the $M - R_o$ plane, as done for DOUBLE EAGLE in Fig.6a and SATURN in Fig.6b. The topology of these contours result from a combination of constant η curves and constant MR_o^2 lines. The lowest yield contour is practically coincident with the $\eta = 0.5$ curve. Higher η curves have a similar parabolic shape but are displaced leftward in the plot. Along a fixed R_o horizontal line, the value of η is large on the left side and the yields are low because one is in the inefficient regime. Moving toward higher masses and lower η, the yields increase because one enters the efficient regime. Finally, at too large a mass $\eta < 1$ and the yields drop off. Lines of constant MR_o^2 run at an angle across the plot as indicated in Fig.6a for one case. The largest value of MR_o^2 occurs in the upper right hand corner. From Fig.5b these lines are also one of fixed kinetic energy. Hence in the lower left region MR_o^2 is small as is E_K. Moving toward the upper right E_K initially increases and then decreases as the peak in the coupled kinetic energy over MR_o^2 is passed. Figs.6a and 6b reflect Fig.2, recognizing that constant η curves are also curves of constant final velocity. One important feature of the J-scaling law to keep in mind is the drop off in yield for the inefficient regime due to a large final radii R_f. Since Fig.6 assumes fixed compression ratio, a larger R_o means a larger R_f, as well as a larger mass break point according to eqn.(7). Thus as R_o is increased at a fixed load mass, one transitions into the inefficient yield regime: the radiation output drops due to a decrease in the plasma density. It is precisely this physical effect that led us to revise the original Whitney-Thornhill scaling law to include a dependency on the final radius in eqn.(3a).

Figures 6a and 6b also list the experimentally measured K-shell yields in kJ within a circle at the appropriate load mass and initial radius. The information was supplied by C. Deeney from Physics International for DOUBLE EAGLE and R. Spielman from Sandia National Labs for SATURN. For DOUBLE EAGLE much of the data lies near a line of constant MR_o^2. Many of the shots were performed under the same initial conditions and the quoted yield is an average of such shots. The K-shell predictions fall short of the observed peak yield by $\sim \frac{1}{3}$, however the trend of a rise and fall over mass loading is consistent with the data. Actually the higher values in Fig.6a represent nearly 100% conversion of kinetic energy into K-shell radiation. The coupled E_K at $MR_o^2 = 0.2$ mg cm^2 is only ~ 30 kJ from Fig.5b. Such a conversion efficiency is impossible, for some of the kinetic energy must be expended in ionizing the plasma. The results

indicate an additional and significant resistive heating phase during pinch assembly for DOUBLE EAGLE, and any yield scaling law based upon kinetic energy per atom alone would necessarily underestimate the experimental values. For SATURN the data represent a more widely dispersed set of initial configurations than for DOUBLE EAGLE. Such data are especially interesting for the present comparison since they cover such a large range in the $M - R_o$ plane and thereby present a challenging test for any model of aluminum K-shell emission. In Fig.6b the peak of the J-scaling law yields compare favorably with SATURN experimental value and the falloff in contour levels from this peak mimics the data, though the contours as a whole are shifted to a larger value of MR_o^2 in comparison with the data. Apparently kinetic energy conversion alone is sufficient to explain the SATURN yields. One could adjust the form of ϵ_L of eqn.(6) to obtain an improved fit for SATURN by reducing the extent of the efficient region, denoted by the straight contour levels. But this function was determined by fitting to multi-zone simulation results for krypton. Since krypton K-shell PRS yields are one of the primary interests in the JUPITER program we leave the present revised J-scaling law as is.

One significant simplification of the present calculations was the use of a fixed initial load inductance L_o. In the actual experiments this value differed for various shots. However the change in L_o for different shots is relatively small compared to $L_o + 3$ nH, and the error introduced by neglecting this change should be considered small given the approximate nature of any scaling law. More importantly, the use of an average L_o value allowed one to use a single calculation at MR_o^2 and obtain many estimates of the yield for various R_o. This approach greatly reduces the time of calculation and readily facilitates the production of contour plots as shown in Fig.6. We will continue to employ this simplifying approach as we look at JUPITER-class generators.

DOUBLE EAGLE
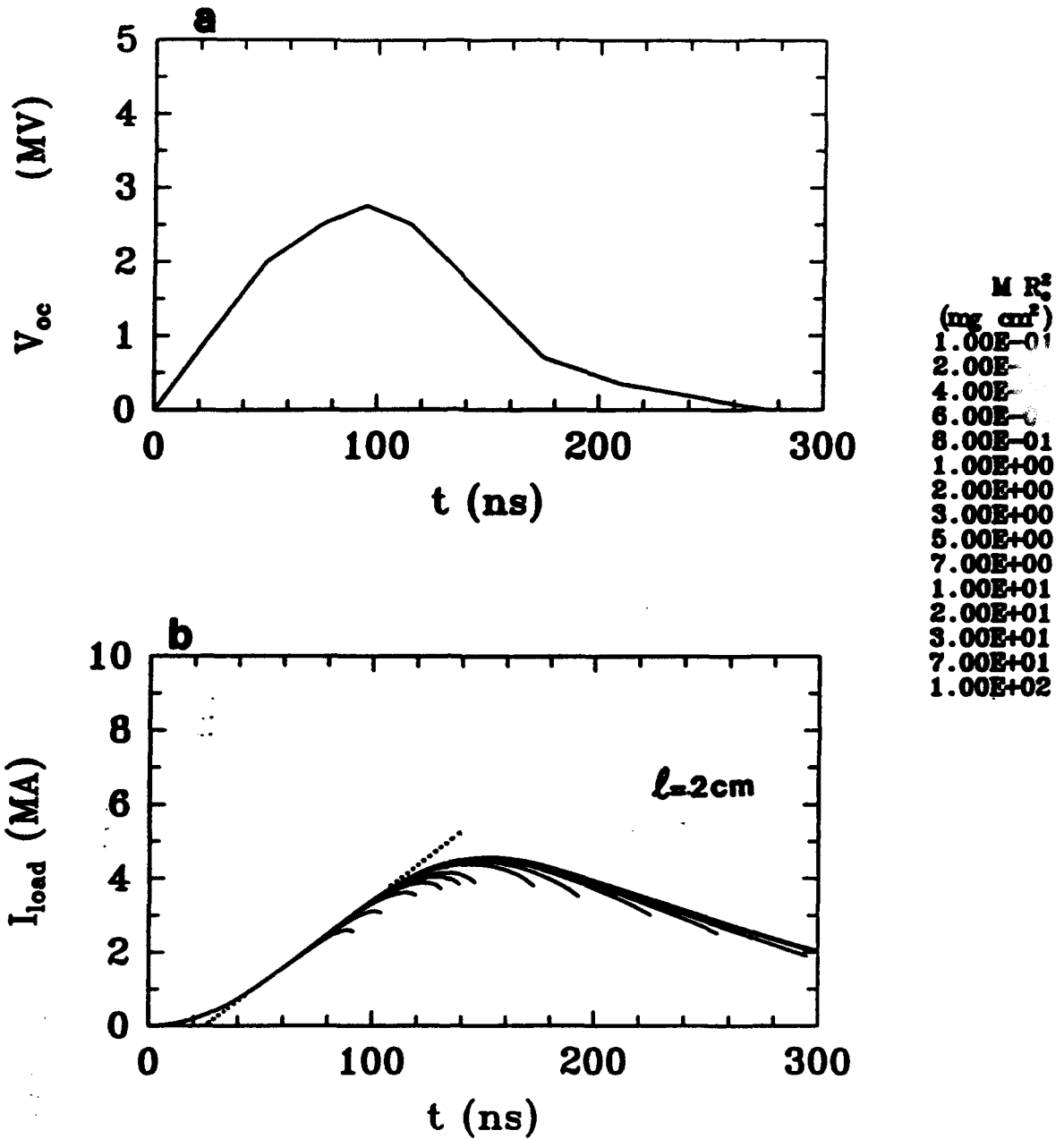
Fig.3(a) The open circuit voltage used to model DOUBLE EAGLE within a Thevenin equivalent circuit. (b) Current profiles of the DOUBLE EAGLE generator for various values of MR_o^2, where M is the load mass and R_o is the initial load radius. Results are for a compression ratio, i.e., final over initial radius, of $1/7$, initial load inductance of 3 nH, and a 2 cm long wire array. When these conditions are fixed the profiles only depend upon the product MR_o^2 within the thin shell approximation for the pinch dynamics.

14

SATURN

a

V_{oc} (MV) vs t (ns)

b

I_{load} (MA) vs t (ns)

ℓ=2cm
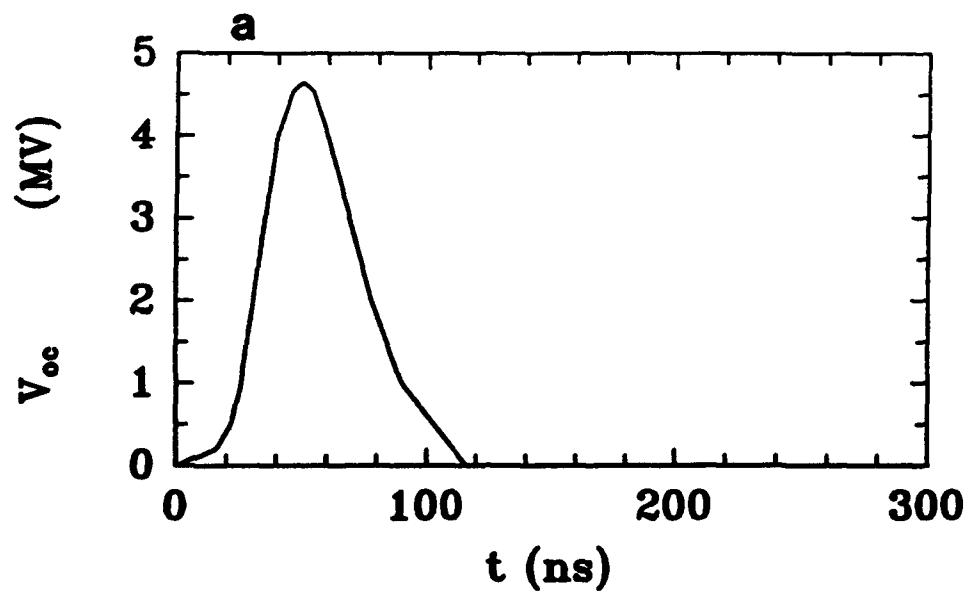
M R²
(mg cm²)
1.00E-01
3.00E-01
6.00E-01
1.00E+00
2.00E+00
3.00E+00
5.00E+00
7.00E+00
1.00E+01
2.00E+01
3.00E+01
4.00E+01
6.00E+01
1.00E+02
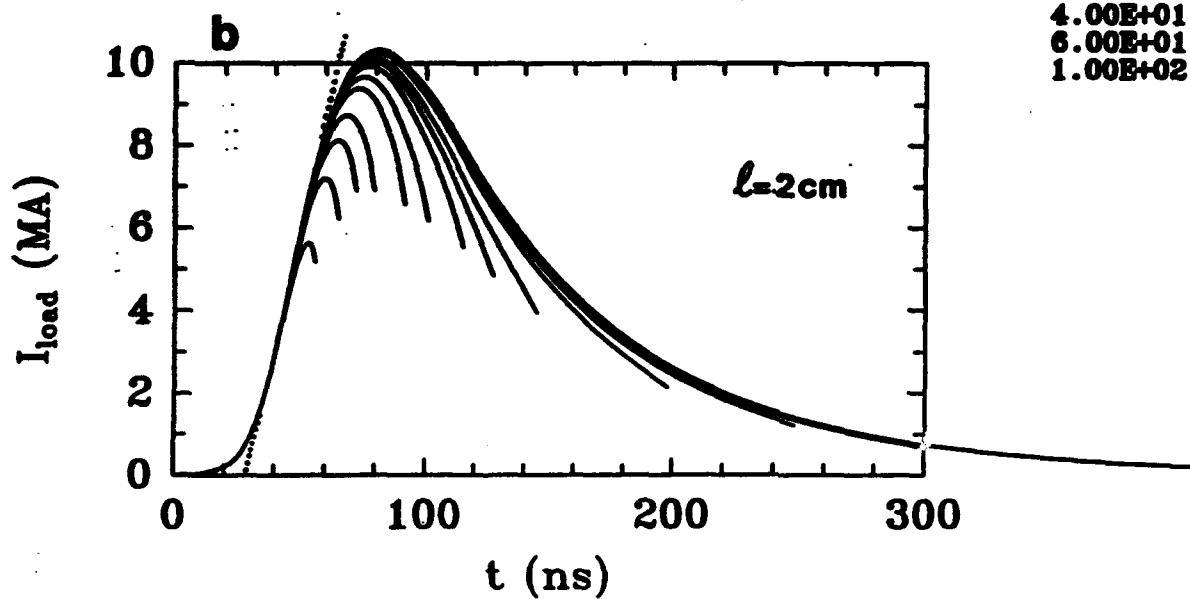
Fig.4 Same as Fig.3 except for SATURN.

15
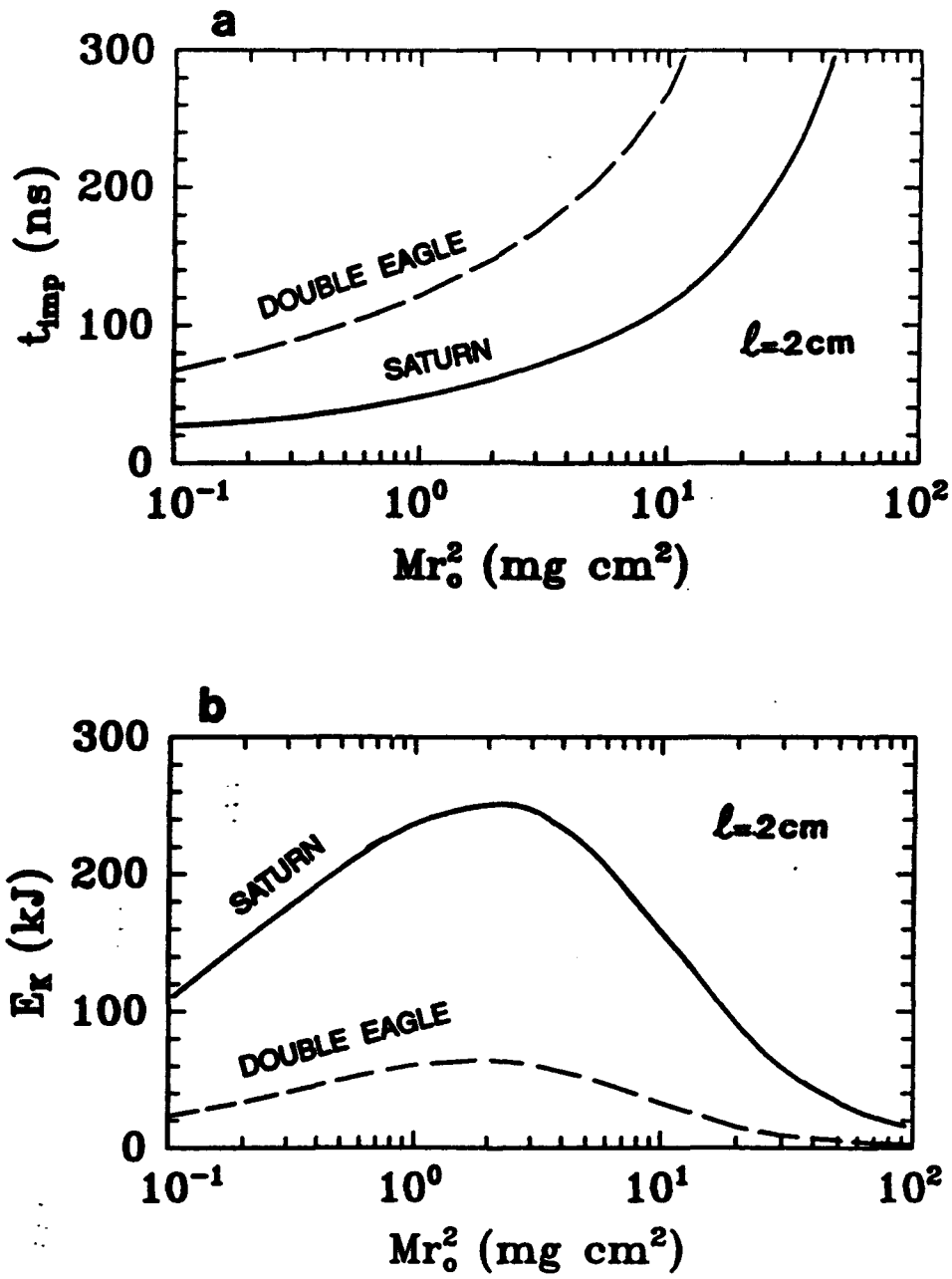
Fig.5(a) Implosion time and coupled kinetic energy (b) as a function of MR_0^2 for DOUBLE EAGLE and SATURN. Initial load inductance, compression ratio, and length are the same as in Fig.3.

16
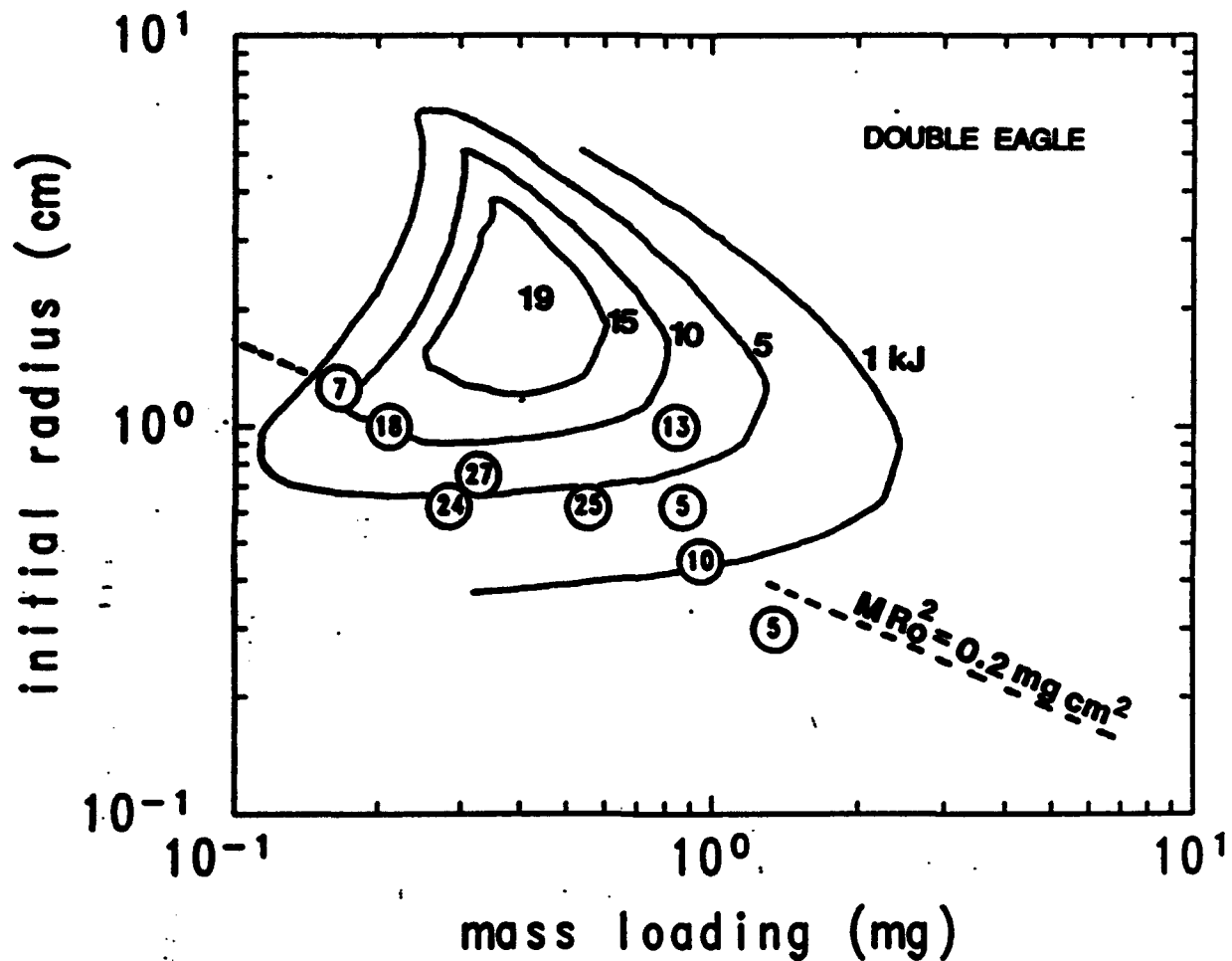
Fig.6(a) Contours of aluminum K-shell yield for DOUBLE EAGLE based on the scaling law. Experimental data in kJ are noted in the circles located at the appropriate $R_o - M$ point. Initial load inductance, pinch length, and compression ratio are the same as in Fig.3.

Fig.6(b) Same as in Fig.6a except for SATURN.

IV. Projected K-Shell Yields as a Function of Load Current

JUPITER is envisioned to have a peak load current of 5 to 7 times that of SATURN. How do the K-shell yields, not only from aluminum but also from higher Z elements, vary with large load currents? To answer this question we employ a analysis similar to the previous section except with a more appropriate circuit model; the voltage risetime of SATURN is only 55 nsec, half the anticipated 100 nsec of JUPITER. Specifically, one of the 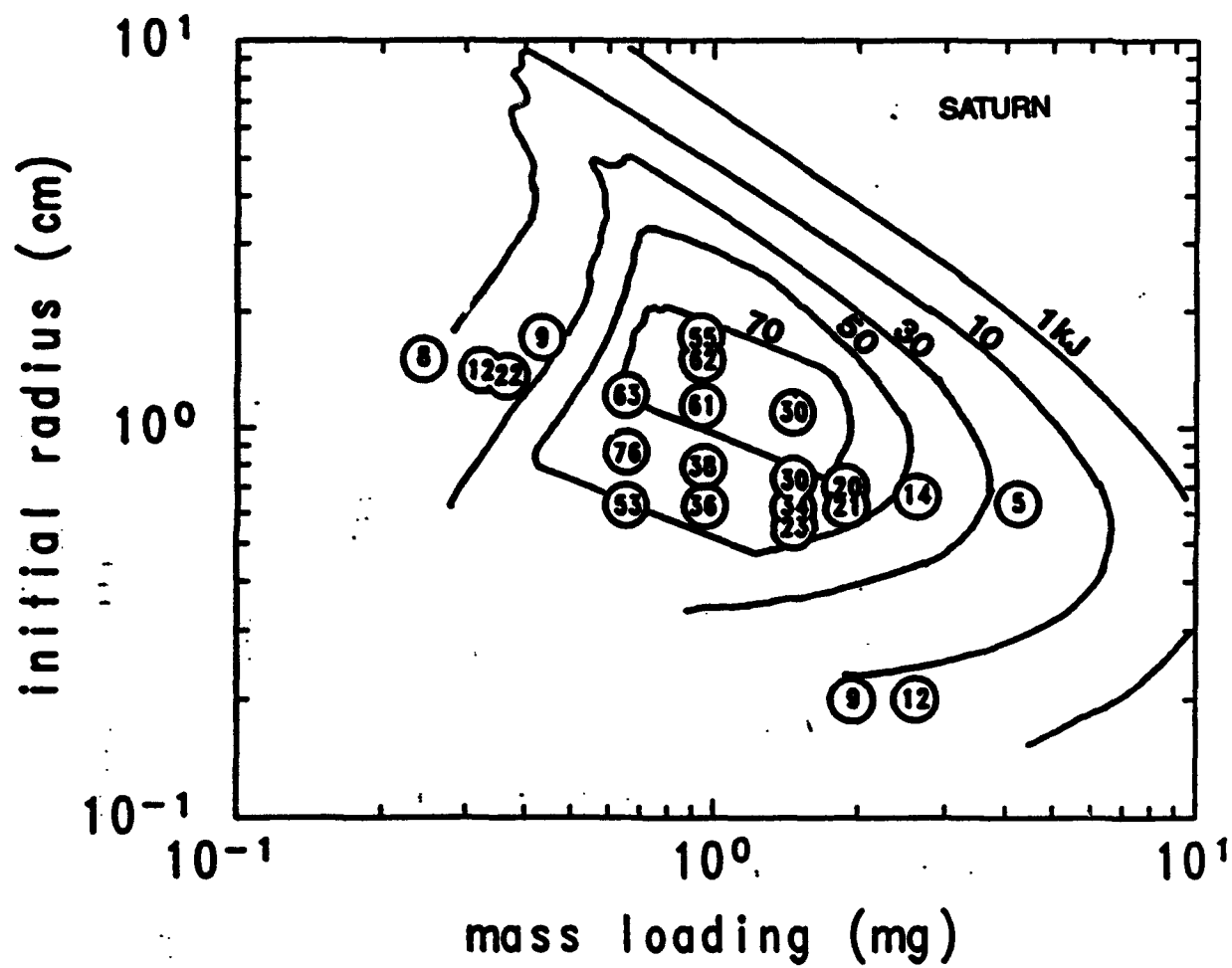early transmission line designs of the linear inductive voltage adder was converted to an equivalent Thevenin circuit. The circuit and forward moving voltage wave V^+ are presented in Fig.7. For the open circuit voltage, $V_{oc} = 2V^+$. The voltage V^+ is measured at the end of a long magnetically insulated transmission line (MITL) of impedance 0.24 Ω. The feed inductance between the MITL and the load is 7.5 nH, and initial load inductance is 2.63 nH. Except for long implosion times ($t_{imp} \gtrsim 200$ nsec), V^+ is unaffected by the load behavior in the LIA design because the voltage source is far removed in time from the load. To achieve a range of peak load currents we multiply V_{oc} by an arbitrary factor α between 0.05 and 2.0 while keeping the impedance and inductance the same. Effectively, for each choice of α we have a different machine characterized by the peak of αV_{oc}.

For each of these machines a search is performed in the $M - R_o$ plane for the maximum K-shell yield of aluminum, argon, krypton, and xenon loads. For reference, the K-shell yield of aluminum means photon energies ≥ 1.6 keV; for argon ≥ 3.1 keV; for krypton ≥ 13 keV; and for xenon $\gtrsim 28$ keV. Figure 8 presents the peak K-shell yields for each of these elements as a function of the peak load current. The initial radii and mass loadings leading to the peak yields are listed beside each data point, and the peak αV_{oc} corresponding to the load current is noted along the abscissa. In this figure the aluminum yield has the classical I^2 dependence of the efficient regime, and argon also reaches the efficient regime above ~ 10 MA. The E_K coupled to the load is shown as a dotted line and in the efficient scaling regime the K-shell yield is $1/3 E_K$, independent of the material in accordance with eqn.(3b). In the terminology of eqn.(1) these elements implode to high η values for this driver. For krypton, however, the yields follow the I^4 regime below ~ 20 MA, then transition to an intermediate dependence, and do not reach the efficient regime until the peak load currents are greater than 100 MA. This transition region for krypton reflects implosions with $\eta \sim 1$ and presents a difficult situation to predict accurately because the yields depend on subtle details of the plasma gradients at implosion. The J-scaling predictions are even more precarious for xenon, where $\eta < 1$. Xenon is included as a element for study because of the radiation requirement for >30 keV photons on JUPITER. Modulo this uncertainty, Fig.8 indicates that to reach 1 MJ of K-shell yield requires ~ 25 MA peak load current for aluminum and argon, ~ 50 MA for krypton, and ~ 90 MA for xenon.

19

The yield results for SATURN lie below the relation between yield and current in Fig.8. The circuit of Fig.7 has a much broader voltage pulse than SATURN and the coupled E_K is also much larger at $I_{peak} \sim$ 10 MA. Even though the yields are similar at peak current between Fig.8 and DOUBLE EAGLE, again the coupled E_K from Fig.7 circuit is larger than on DOUBLE EAGLE. This points out the limitation of trying to study yields in a machine independent manner as implied in Fig.8. We thus next turn to specific JUPITER designs for yield estimates.

$$R = 0.24\Omega \qquad L = 7.503 \text{ nH}$$

$$V_{oc} \qquad L_o = 2.63 \text{ nH}$$
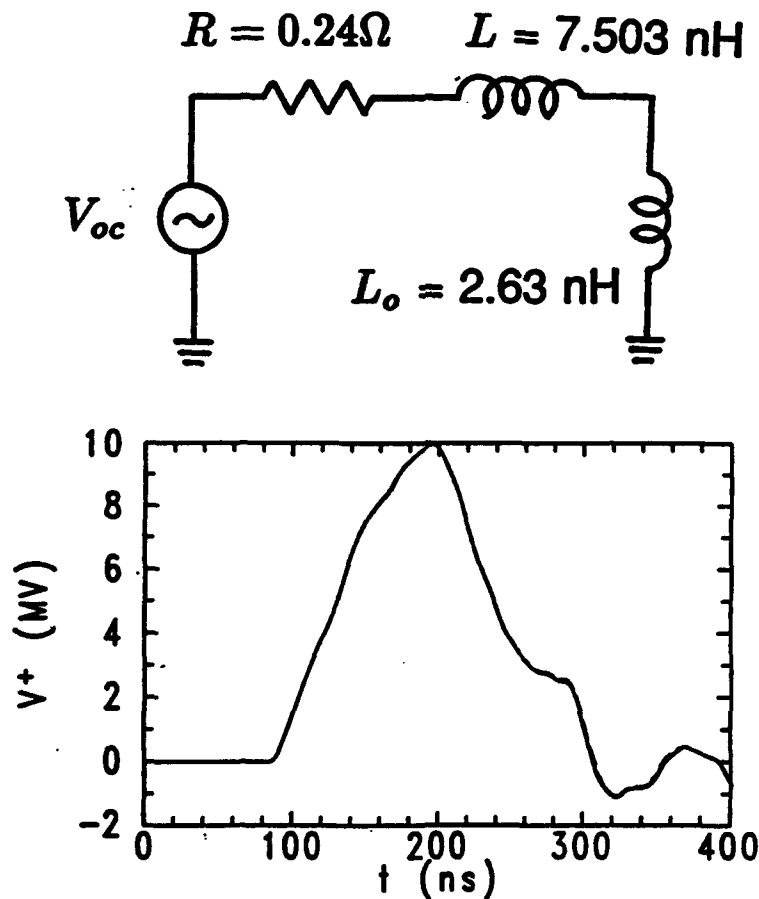
Fig.7 The Thevenin equivalent circuit and the foward moving voltage wave V^+ at the end of the long MITL for an early Voltage Adder JUPITER design. Twice V^+ equals the open circuit voltage V_{oc}.

20
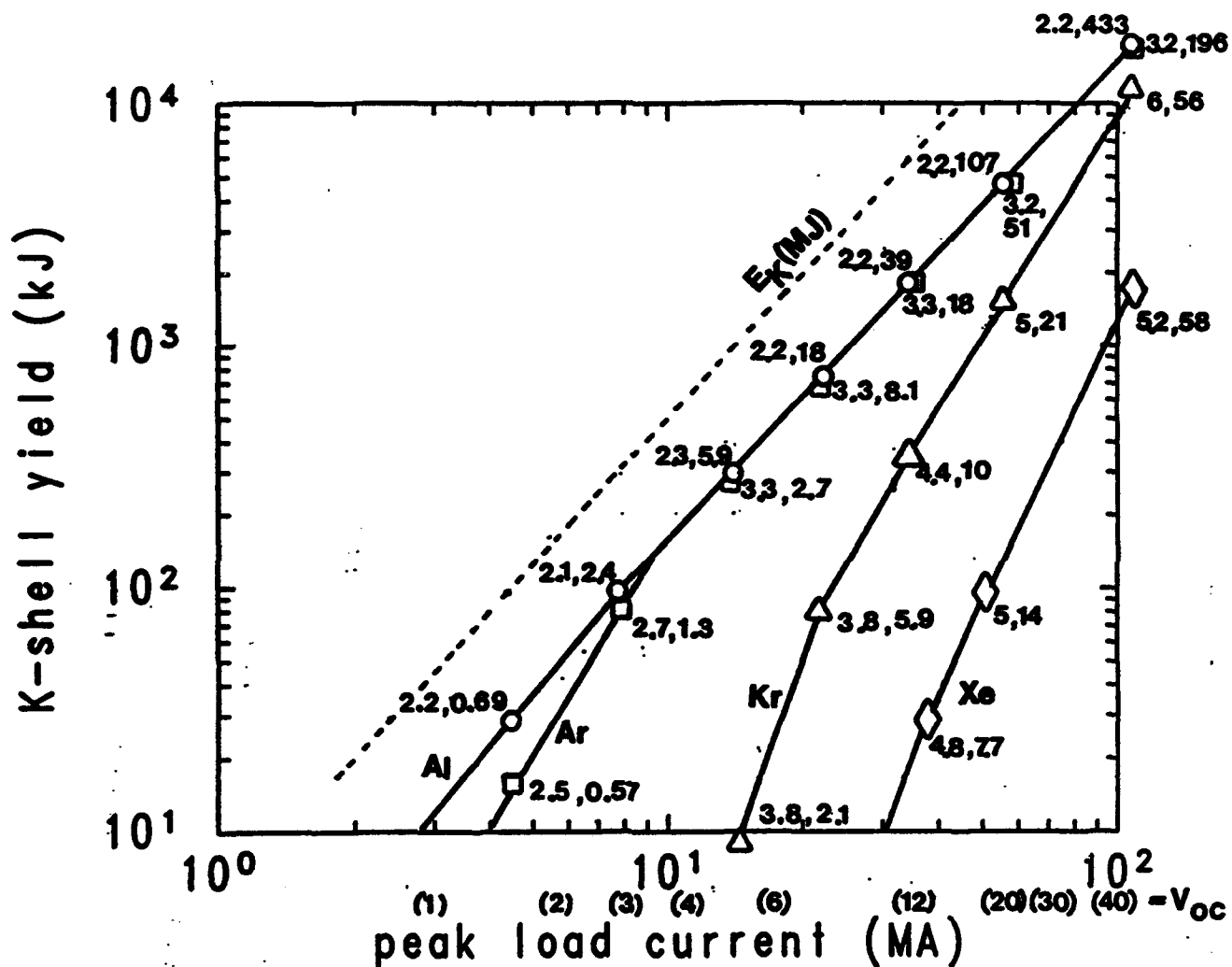
Fig.8 Peak K-shell yields from the scaling law for aluminum (>1.6 keV), argon (>3.1 keV), krypton (>13 keV), and xenon ($\gtrsim$28 keV) as a function of the peak load current from the circuit of Fig.7. The open circuit voltage from Fig.7 is magnified to obtain varying peak load currents. The peak V_{oc} is noted along the abscissa. The dotted line gives the coupled kinetic energy as a function of the current. Each point is labeled as (R_o in cm, M in mg). Results are for a compression ratio $R_f/R_o = {}^1\!/_7$, initial load inductance of 2.63 nH, and a 4 cm long load.

V. Projected K-shell Yields for the Standard LIA and IES JUPITER Circuit Designs.

During the span of the Jupiter Design Option Study Team (JDOST) from July 1993 to January 1994, a number of generator designs have been proposed and have undergone significant and continuous evolution. Rather than present the many yield studies undertaken during this period as part of an historical development, we will concentrate on the latest designs for the LIA and the modular IES as of January, 1994. The transmission line circuit used in the present report to model the 4 cells/module, 30 module LIA with a low inductance, 4-slot front end is presented in Fig.9a. Several items should be noted regarding this simplified circuit. They were adopted primarily to speed up calculations over large domains of parameter space.

(i) The 30 modules were added in parallel to the front end convolute.

(ii) The length of each element is rounded to an integral number of nanoseconds while the impedance remains unchanged. This increases the front end inductance by a negligible 0.0027 nH compared to the exact circuit.

(iii) The inductance of the double post-hole convolute, final feed, and half inch pinch pedestal are all added to the final MITL element, without increasing its time length. The total inductance for this combined element, which will be termed the feed inductance

$$L_f = 1.4 + 0.36 + \ln\left(\frac{6.0}{(R_o + 0.5)}\right) + \ln\left(\frac{(R_o + 0.5)}{R_o}\right) \quad \text{nH,} \qquad (15)$$

ranges from 2.86 nH for $R_o = 2$ cm to 1.94 for $R_o = 5$ cm as shown in Table I. The value of L_w used to generate a particular graph is listed in the corresponding caption. Because peak yields are found to occur at large initial radii, we will generally employ the feed inductance appropriate to $R_o = 5$ cm. Figs.10h and 11h discussed below show the small effect upon the yields of including the R_o dependency in the inductance L_f. The expediency gained by ignoring the R_o dependency in L_f has been explained at the end of Section III. Since the increase in inductance as the pinch implodes can be $\geq$ the fixed front end inductance, the dependency of the initial load inductance on pinch length,

$$L_w = 2\ell \ln\left((R_o + 0.5)/R_o\right) \quad \text{nH,} \qquad (16)$$

is accounted for in all calculations. Of course so is the change in the load inductance as the implosion proceeds, in the manner of eqn.(12). It is recognized that the gap size of 0.5 cm between the load and the return current radius is clearly too small for gas puffs, and possibly also for wire-array loads, on either design. As this value was chosen by Sandia for IES studies of energy coupling, we adopted it for consistency on both machines.

Table I. Final Feed L_f and Initial Load Inductance L_w.

$L_f + L_w$ (nH)	$\ell = 2$ cm	4 cm	6 cm
$R_o = 2$ cm	2.86+0.89	2.86+1.78	2.86+2.68
5 cm	1.94+0.38	1.94+0.76	1.94+1.14

(iv) No losses are included in the present calculations, either in the marx spark gaps, gas and water closing switches, MITL transition e^-, convolute, or final feed resistance. Incorporation of loss models into our transmission line code is a future objective.

(v) The transmission line does not go all the back to the marx banks but starts at the intermediate store with 41.36 MJ of electrical energy. When all the losses are included the marx banks initially store 94 MJ and the intermediate store reaches 69 MJ. The lower energy for the intermediate store is suggested by Ian Smith of the LIA design team to balance the neglected power losses.

The transmission line circuit used in the present report to model the 60 module IES with a similar low inductance, 4-slot front end is presented in Fig.9b. Again there are a number of items to be noted.

(i) The 60 modules were added in parallel to the front end convolute.

(ii) The length of each element is rounded to an integral nanosecond length but the impedance is adjusted so that the inductance of each element remains constant.

(iii) As above, the inductance of the double post-hole convolute, final feed, and pedestal are added to the final MITL element prior to the load. The pinch length is again accounted for in the load inductance.

(iv) No losses are included, except across the POS (see below).

(v) The pulse shaping capacitor actually forms a "T" with the transmission line but we have treated it in series. Comparisons of SCREAMER circuit code calculations at Sandia with the present model show small but acceptable differences.

(vi) The linear tapered storage inductor is broken into three segments each of constant but decreasing impedance such that the total inductance is conserved.

(vii) The plasma opening switch is treated as time varying shunt resistor with energy losses. The resistance R_{POS} satisfies the Z_{flow} model of Mendel et al., [Ref.9]:

$$Z_{flow} = \frac{V_{POS}}{\sqrt{|I_{up}^2 - I_{dn}^2|}} = R_{POS}\sqrt{\frac{|I_{up} - I_{dn}|}{I_{up} + I_{dn}}}. \tag{17}$$

Here V_{POS} is the voltage across the switch, I_{up} and I_{dn} are the upstream and downstream currents surrounding the POS so that $V_{POS} = R_{POS}I_{POS} + R_{POS}(I_{up} - I_{dn})$. The flow impedance Z_{flow} is specified by the conduction time t_{open}, the duration of opening Δt_{open}, and Z_{flow}^{max} listed in the Fig.9b through

$$Z_{flow}(t) \quad = \quad \begin{cases} 0,, & \text{for} \quad t \le t_{open}; \\ Z_{flow}^{max}\left(1 - \dfrac{t}{\Delta t_{open}}\right), & \text{for} \quad t_{open} \le t \le t_{open} + \Delta t_{open}; \\ Z_{flow}^{max}, & \text{for} \quad t \ge t_{open} + \Delta t_{open}. \end{cases} \qquad (18)$$

The listed conduction time corresponds to the POS opening at a storage inductor current of 90 MA. For the present implementation of the Z_{flow} model, the switch is not crowbared ($R_{POS} \to 0$) if the voltage across the POS reverses. Instead $R_{POS} \to \infty$ when $I_{up} = I_{dn}$, as Z_{flow} remains finite.

In Figs.9a and 9b the noted times for the closing and opening of the switches are measured from the instant when the energy begins to flow forward out of the first element on the left. Thus for the IES the effective conduction time of the plasma is shorter than the listed t_{open} of the figure due to the time delay in the transmission line between the first element and the switch. Measured from the time when the POS first carries at least 1 MA, the conduction time for IES-4 of Fig.9b is $\sim 0.7\ \mu s$.

To study these JUPITER circuits we perform a similar analysis as was done for DOUBLE EAGLE and SATURN in Section III. The imploding plasma thin shell model of eqn.(11) still holds but the circuit model of eqn.(12) is replaced with a transmission line calculation. The transmission line model follows the forward and backward propagating voltage waves assuming only transverse electromagnetic modes are present. Circuit elements have associated transit times Δt such that a line element of impedance Z has an inductance $Z\Delta t$ and a capacitance $\Delta t/Z$. Wave propagation across junctions between line elements is solved through reflection and transmission coefficients derived from Kirkhoff's laws. The general technique is similar to the BERTHA code used at NRL [Ref.10], however, the junction at the dynamic load is treated implicitly to ensure strict conservation of electrical + plasma energy.

For a given machine, pinch length ℓ, initial inductance L_w, and compression ratio R_f/R_o, the pinch dynamics is only a function of MR_o^2, as in eqn.(14). Hereinafter the compression ratio in the calculations is fixed at $1/10$. The final feed + initial load inductance will be listed in the figure captions as L_w from Table I. Figures 10a and 10b show, respectively, the load current and the coax MITL voltage for the LIA with a 4 cm long pinch over a range of MR_o^2 values. The time $t = 0$

24

on the plots of Fig.10 corresponds to the time of PFL switch closing in Fig.9a. The MITL voltage only takes $\sim$30 ns to reach a 7 MV plateau and stays positive for $\sim$110 ns. The back emf-voltage generated by the motional impedance of the imploding plasma [the $\dot{x}/x$ term in eqn.(12)] is clearly demonstrated in Fig.10b. For an inductive short circuit load, the current rises to a peak value of $\sim$85 MA about 80 ns after the current first starts to flow into the load. The implosion time, calculated in the manner described in Section III, is shown in Fig.10c for various pinch lengths on the LIA. For a fixed length, t_{imp} is a monotonically increasing function of MR_o^2, but shorter lengths have a larger t_{imp} at the same MR_o^2. The load kinetic energy at implosion, E_K in Fig.10d, displays a definite peak at $MR_o^2/\ell \sim 200$ mg cm, for pinch length ℓ. The peak E_K increases with length, but slower than linearly. That is, the total pinch E_K increases with length, but shorter pinches produce more E_K per unit length. This feature impacts the optimal yielding pinch length for different Z as we shall show below. The excursion to large voltages at implosion in Fig.10b is important only for $MR_o^2 \leq 500$ mg cm^2, which is below the value of MR_o^2 where the kinetic energy peaks for $\ell = 4$ cm. For $\ell = 2$ cm the large voltage excursion is also found to occur below the MR_o^2 producing the peak E_K.

K-shell yields for the LIA based upon the J-scaling law can be calculated using the same formalism discussed at the end of Section III. A contour map of krypton K-shell yields over the $M - R_o$ plane is shown in Fig.10e. The peak yield is nearly 3 MJ at $R_o = 5.8$ cm and $M = 25.4$ mg. Consider a horizontal line of fixed radius in Fig.10e and determine the peak yield for that radius. The dependence of this krypton peak yield on initial radii is displayed in Fig.10f, along with the results for Ar and Xe. Note the broad range about $R_o \sim 5$ cm where the K-shell yields are near their maximum. While Fig.10f is for 4 cm long pinches, Fig.10g shows the variation of the peak K-shell yields at each initial radius as the pinch length changes from 2 to 6 cm. On JUPITER, argon implosions can have many times the energy needed to reach the K-shell ionization stage. Hence argon is in the efficient scaling regime and according to eqn.(3b) $Y_K(Ar) \propto E_K$. Since E_K increases with length (from Fig.10d), longer pinches in Fig.10g lead to optimal yields for low Z elements like argon. On the other hand, xenon implosions on JUPITER will be energy poor, i.e., the η of eqn.(1) < 1. Because the xenon K-shell yield scaling is in the inefficient I^4 or M^2 regime, shorter pinches which produce a higher E_K/ℓ lead to better K-shell yields as in Fig.10g. In essence, large E_K/ℓ for xenon lead to higher η and a larger $\epsilon_L(\eta)$ in eqn.(3a). The yield drop off at large R_o reflects the larger stagnation radius R_f and a lower yield by eqn.(3a). Krypton is a transition material for JUPITER, $\eta \sim 1$ for the optimal cases, and the peak yield is not a strong function of the length. Up to this point the calculations have used a final feed inductance from Table I appropriate to an initial pinch radius of 5 cm. To verify our earlier claim of insensibility to the variation in the final feed inductance, we present in Fig.10h a comparison between yields based

upon a final feed + load inductance of 1.94+0.76 nH (case a), and 2.86+1.78 nH (case b). The numbers are taken from Table I for 4 cm length pinches but different R_o. Clearly the differences are not large, but there is a systematic trend for the LIA in that the larger inductance case b always presents slightly larger yields.

For detailed study, Table II contains specific data on the peak Y_K at several initial radii along with the associated t_{imp}, M, and E_K. Since argon is in the efficient radiation regime on JUPITER, the peak yield scales with the kinetic energy which is a function of MR_o^2. The first two entries in the argon group for each pinch length ℓ show the range in initial radii and masses which lead to the same peak yield. For the krypton and xenon loads, the first listing in each group of lengths is the peak yield over all radii. Rayleigh-Taylor instabilities may inhibit the utility of large radii implosions, so yields are also listed for radii $\leq$ 4 cm.

A analogous set of the above graphs is presented in Fig.11 for the standard IES JUPITER design. The $t = 0$ point in Figs.11a and 11b correspond to the time when the POS of Fig.9b begins to open. If one lines up V_{MITL} from the LIA in Fig.10b and V_{POS} from the IES in Fig.11b such that the initial voltage rise overlaps, one finds that it takes only 35 ns for the LIA MITL voltage to reach its plateau value of 7 MV, but 50 ns for the IES voltage to reach a similar plateau. Furthermore, the back reaction of the load through its motional impedance is more prominent for small MR_o^2 on the LIA than on the IES. This difference reflects the assumption that Z_{flow} remains constant after POS opening and as the current through the switch rises near t_{imp} the voltage V_{POS} must decrease by eqn.(17). The load current profiles of the IES in Fig.11a display a knee after the initial rapid rise, unlike I_{load} on the LIA. Hence the time to peak current is longer on the IES than on the LIA, especially for large MR_o^2 values. For instance, the time to peak load current is $\sim$100 ns on the IES for $MR_o^2 = 10^3$ mg cm^2, while it is only 70 ns on the LIA for the same value. The implosion times and E_K are presented in Fig.11c and 11d, respectively, for several pinch lengths. t_{imp} for the IES is about 15 nsec longer than on the LIA for the same MR_o^2, as long as $MR_o^2 < $ a few thousand. Above this value the implosion times are less on the IES than the LIA. The peak E_K at each length studied is nearly the same on the IES design as on the LIA design, but for the IES the peak E_K roughly follows $MR_o^2/\ell \sim$ 300 mg cm. Thus the IES reaches its peak E_K at a larger MR_o^2 value than on the LIA. This behavior suggests that the peak yields for high Z materials will occur at larger initial radii for the IES machine. Another difference between the E_K on the LIA and on the IES is the definite peak in E_K over MR_o^2 on the LIA, while the E_K for the IES shows a secondary peak at large MR_o^2. The secondary peak would not appear if the POS is crowbared after V_{POS} first reverses sign. This structure in the kinetic energy curves at large MR_o^2 is reflected in the krypton K-shell yield contours of Fig.11e. The peak krypton K-shell yield, as well as the R_o and M leading to it, for the IES in Fig.11e and for the LIA in Fig.10e are fairly similar. But note that

a given yield contour extends to smaller radii for the LIA than for the IES. This difference can be seen by comparing the peak K-shell yields at each R_o in Figs.10f and 11f. While the peak Y_K over all R_o are about the same for both machines and occur between 5 and 6 cm, the LIA can approach its maximum yield with R_o as small as 4 cm, while the peak yields for the IES rapidly drop off below 4 cm for Kr and Xe. Fig.11g shows the similar trend as for the LIA, i.e., the pinch length for the low Z elements should be large, while it should be short for the highest Z elements. Again, Fig.11h shows that the present study is not sensitive to the exact front end inductance of Table I. The higher inductance setting of Table I (case b) produces a slightly lower peak yield than the lower inductance case a. It is interesting to note that this is the exact opposite from what was found for the LIA and suggests a different dependence on the front end inductance of the two machines.

Table III list analogous results for the IES as Table II for the LIA. One sees that the peak yield and conditions are fairly similar on the two design, but if the loads are limited to $R_o \leq 4$ cm the IES peak yields are significantly less than those from the LIA.
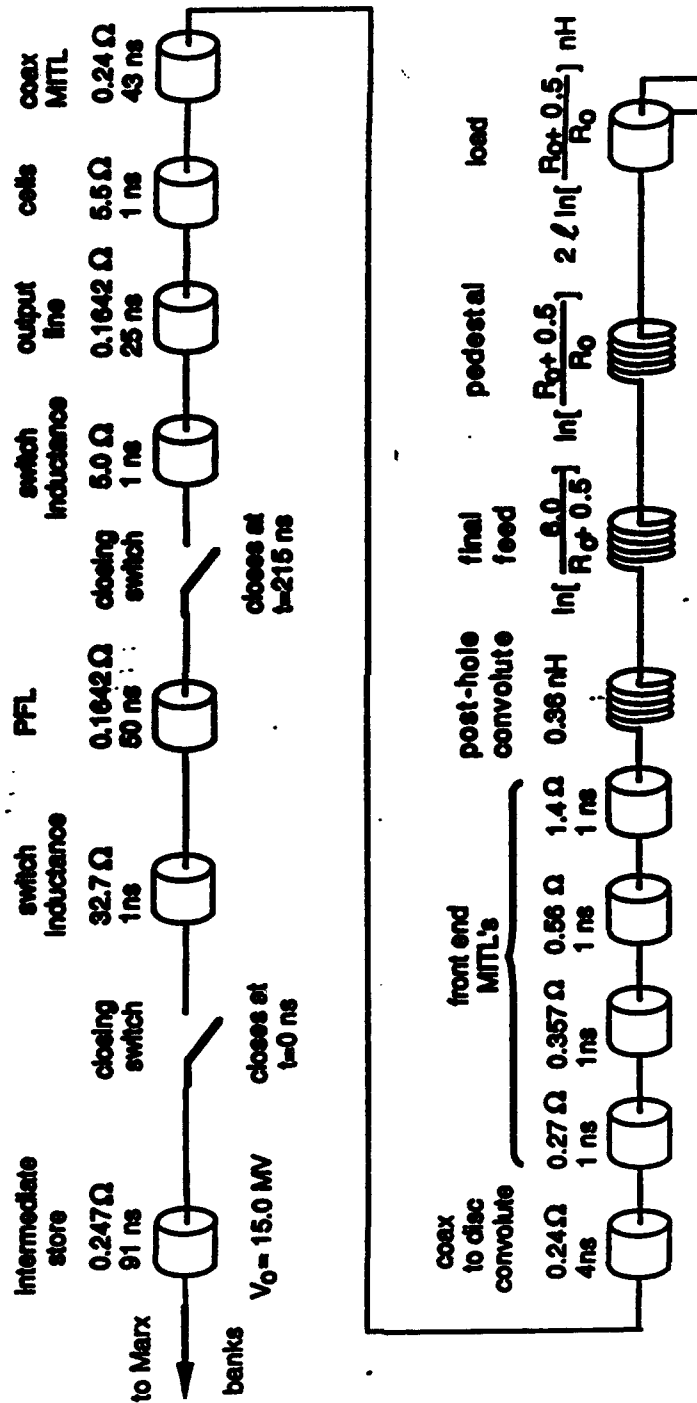
LIA-4 (1/5/94)

Fig.9(a) Transmission line circuit used to model the Linear Inductive Voltage Adder (LIA) design for JUPITER. In this circuit the 4 cells/module, and 30 modules are combined in parallel with the low inductance, 4-slot front end.

IES-4 (1/1/94)

Marx banks

pulse shaping capacitor

MFI inductance

Linear Tapered Storage Inductor

2.688E-5 Ω
1 ns

11.5 Ω
1 ns

0.0109 Ω
192 ns

0.0107 Ω
1 ns

0.3181 Ω
1 ns

0.5633 Ω
1 ns

0.239 Ω
17 ns

0.220 Ω
17 ns

0.200 Ω
17 ns

$V_0 = 2.7$ MV
$E_0 = 136$ MJ

closes at
t=0 ns

R = 2.77E-6 Ω
R = 3.4 Ω

R = 1.7 Ω

POS   fast field   feed   coax to disc   front end   post-hole   final   pedestal   load
       coil   convolute   MITL's   convolute   feed

0.415 Ω   0.125 Ω   0.24 Ω   0.225 Ω   0.357 Ω   0.56 Ω   1.4 Ω   0.36 nH $\ln\left[\frac{8.0}{R_0 + 0.5}\right]$ $\ln\left[\frac{R_0 + 0.5}{R_0}\right]$ $2\ell \ln\left[\frac{R_0 + 0.5}{R_0}\right]$ nH
4 ns   7 ns   4 ns   1 ns   1 ns   1 ns   1 ns

$Z_{flow} = 0.1333$ Ω
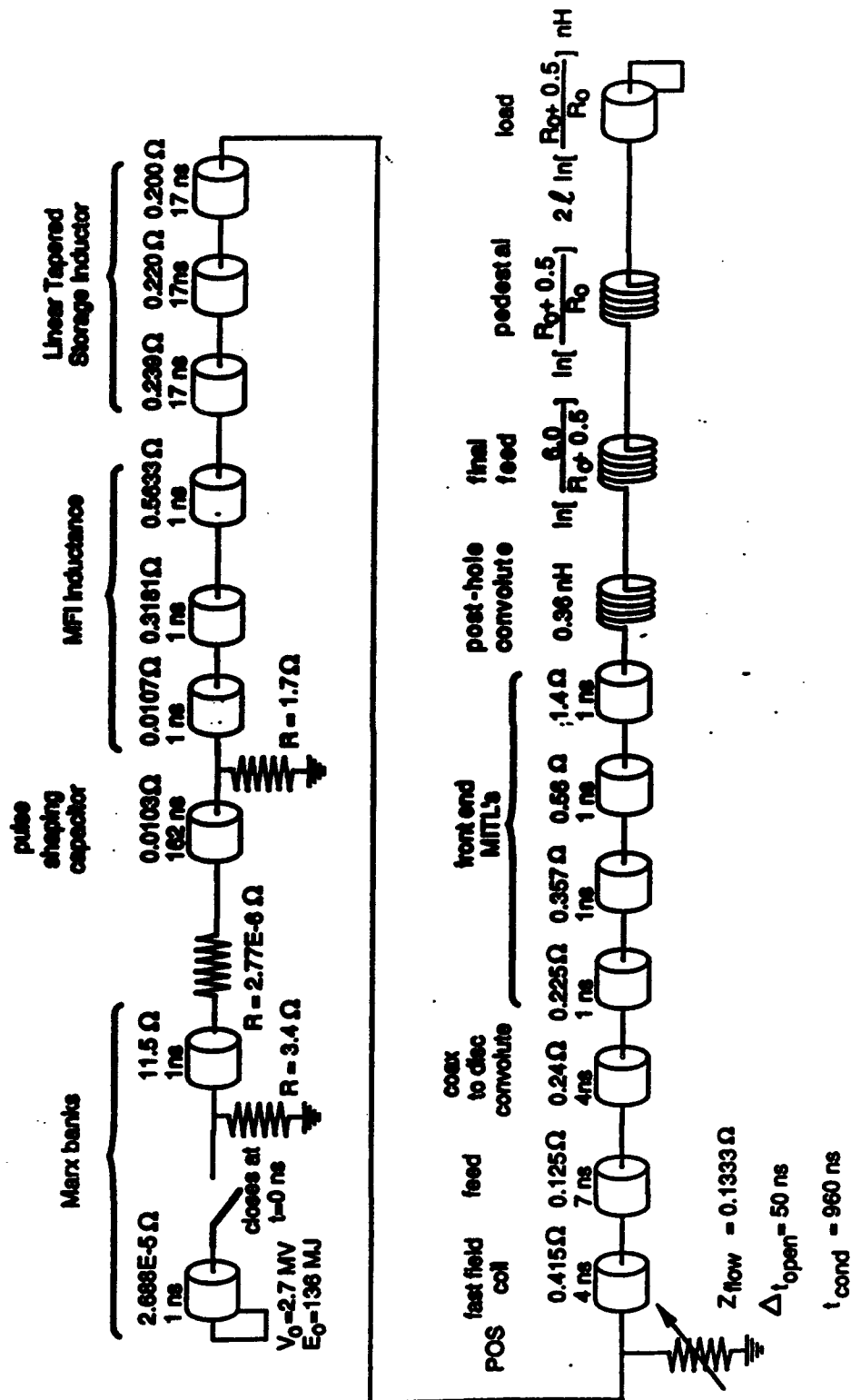$\Delta t_{open} = 50$ ns
$t_{cond} = 960$ ns

Fig.9(b) Transmission line circuit used to model the modular Inductive Energy Store (IES) design for JUPITER. In this circuit 60 modules, each containing a plasma opening switch (POS) are combined in parallel with the low inductance, 4-slot front end.
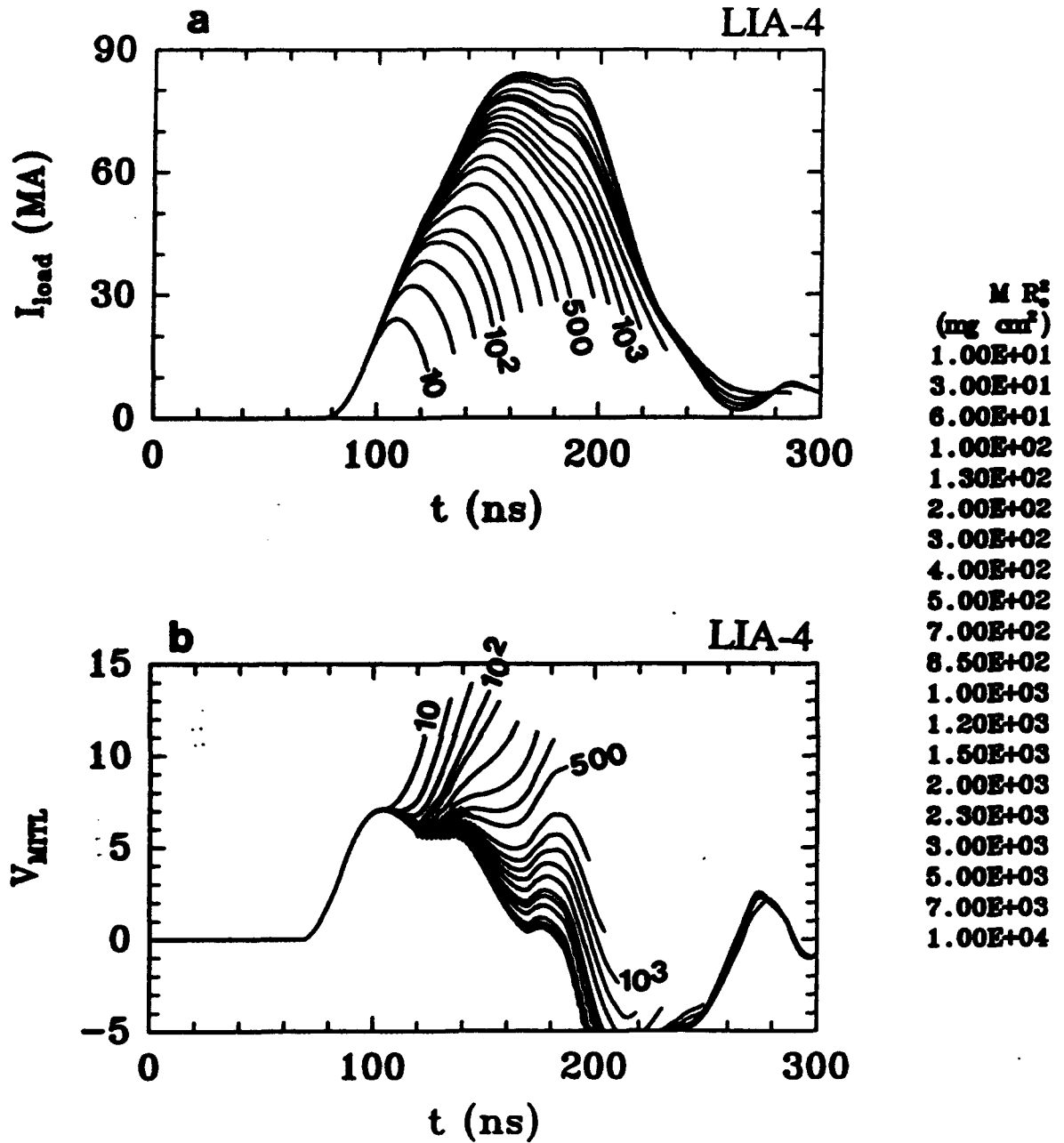
29

a LIA-4

I_{load} (MA)

90

60

30

0

10 10^2 500 10^3

0   100   200   300

t (ns)

b LIA-4

V_{MITL}

15

10

5

0

-5

10^2

10

500

10^3

0   100   200   300

t (ns)

$M R_o^2$
(mg cm^2)
1.00E+01
3.00E+01
6.00E+01
1.00E+02
1.30E+02
2.00E+02
3.00E+02
4.00E+02
5.00E+02
7.00E+02
8.50E+02
1.00E+03
1.20E+03
1.50E+03
2.00E+03
2.30E+03
3.00E+03
5.00E+03
7.00E+03
1.00E+04

Fig.10(a) The current profiles and coax MITL voltages (b) for LIA-4 for various values of $M R_o^2$. The time $t = 0$ corresponds to the closing of the PFL switch. The pinch length is 4 cm, and the final feed inductance $L_f = 1.94$ nH from Table I. For all of the remaining figures the compression ratio $R_f / R_o = 1/10$.
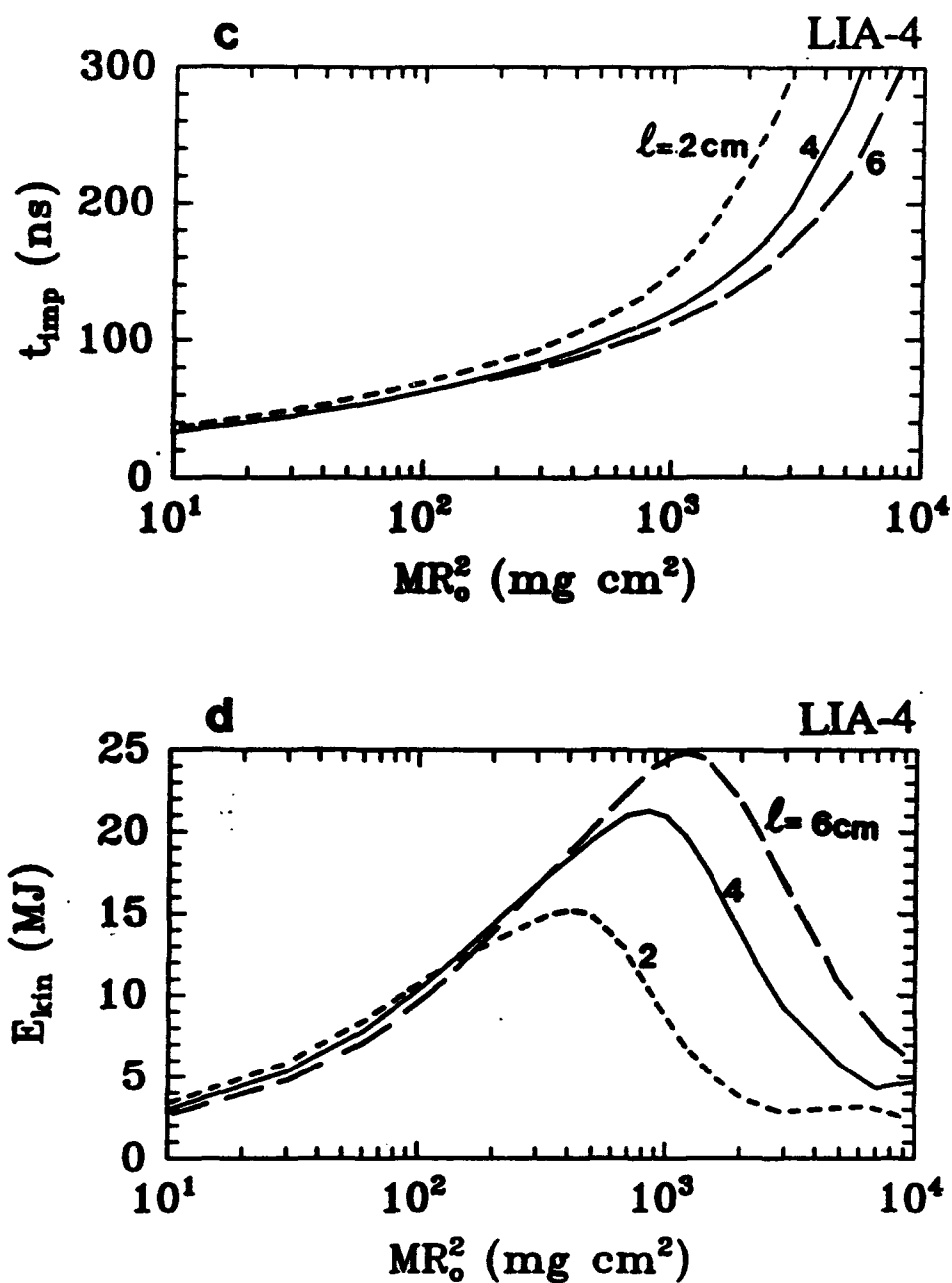
Fig.10(c) The implosion times for three pinch lengths (ℓ) on LIA-4 as a function of MR_o^2. (d) The plasma kinetic energy at implosion for the same lengths. ($L_f = 1.94$ nH).
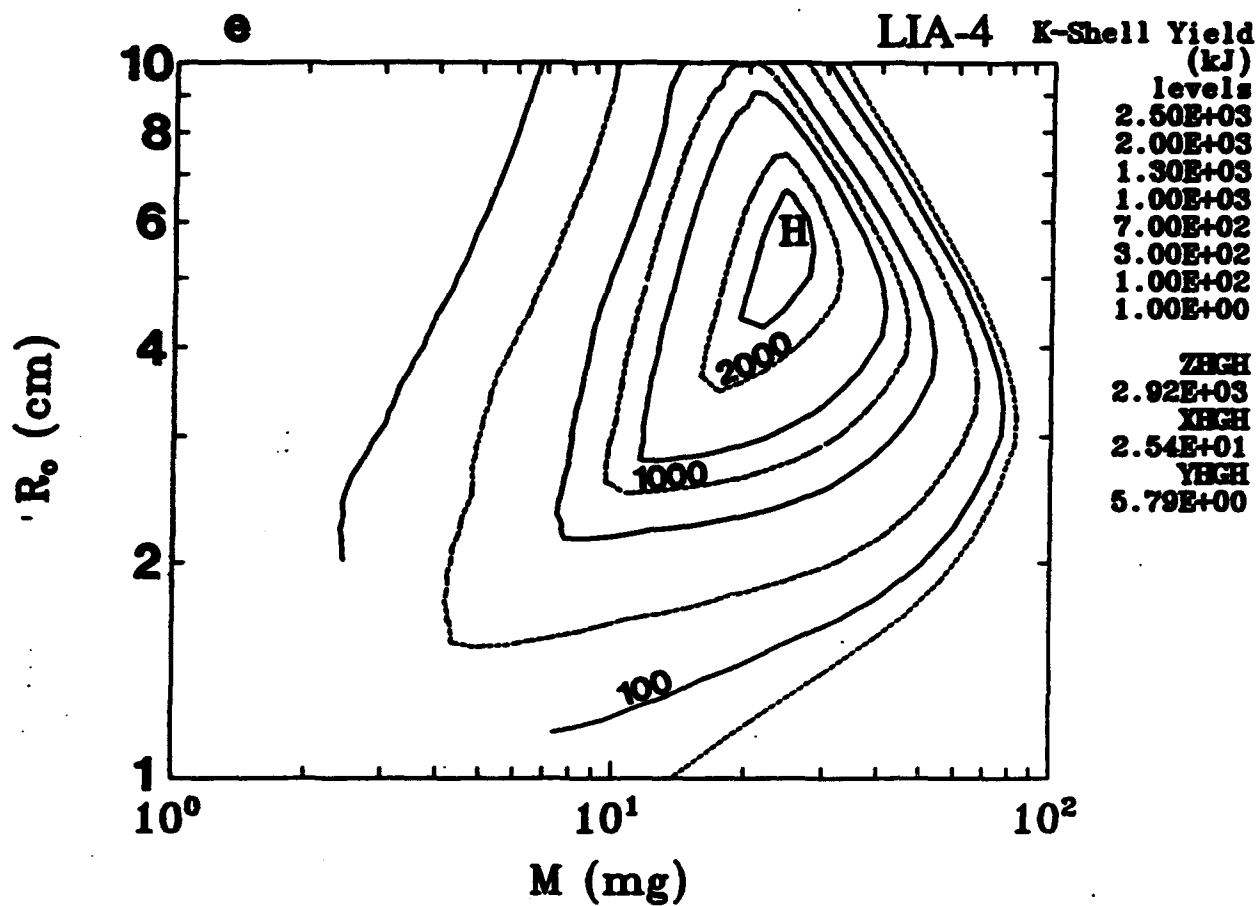
31

Fig.10(e) Contours of total krypton K-shell yield based on the scaling law for the LIA-4. Load conditions are the same as in Fig.10a.
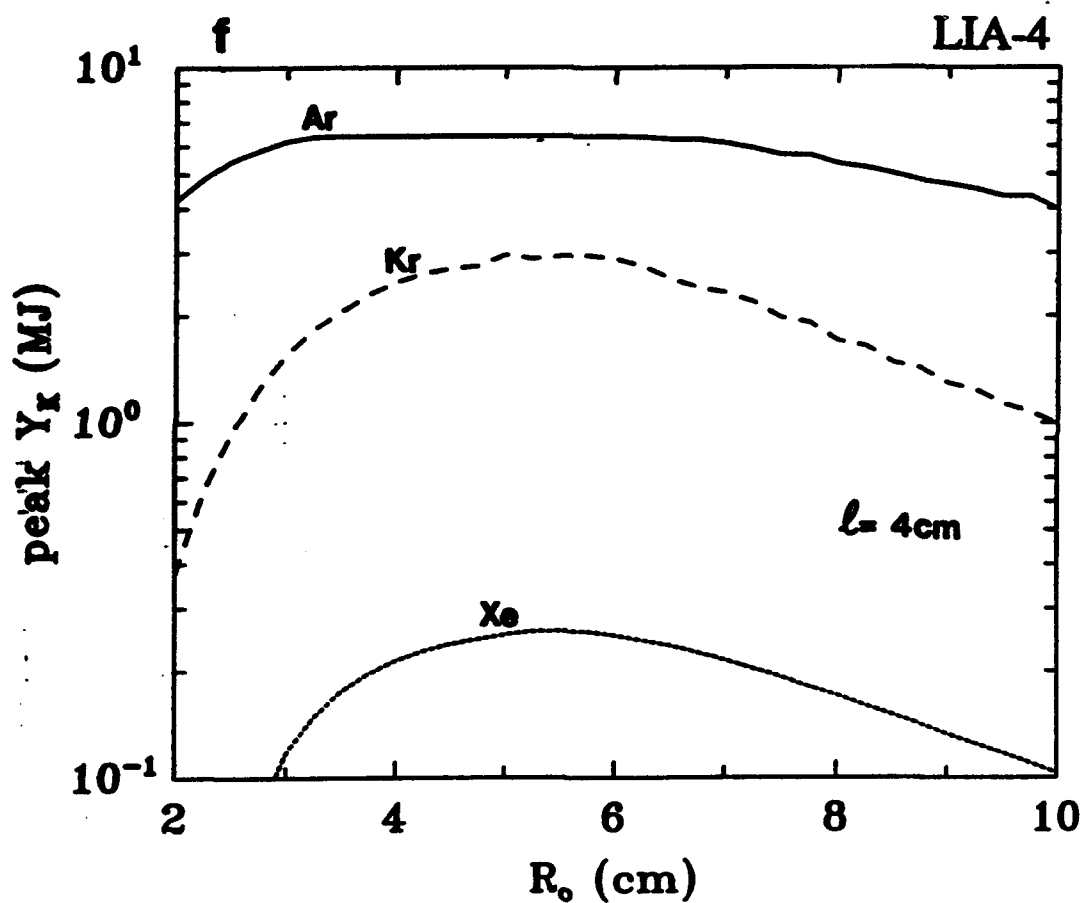
Fig.10(f) Peak K-shell yields at different initial radii for Ar($>$ 3 keV), Kr($>$ 13 keV), and Xe($\gtrsim$28 keV) on LIA-4. Note that the peak yields are close to their maximum, even with R_o as small as 4 cm. Load conditions are the same as in Fig.10a.
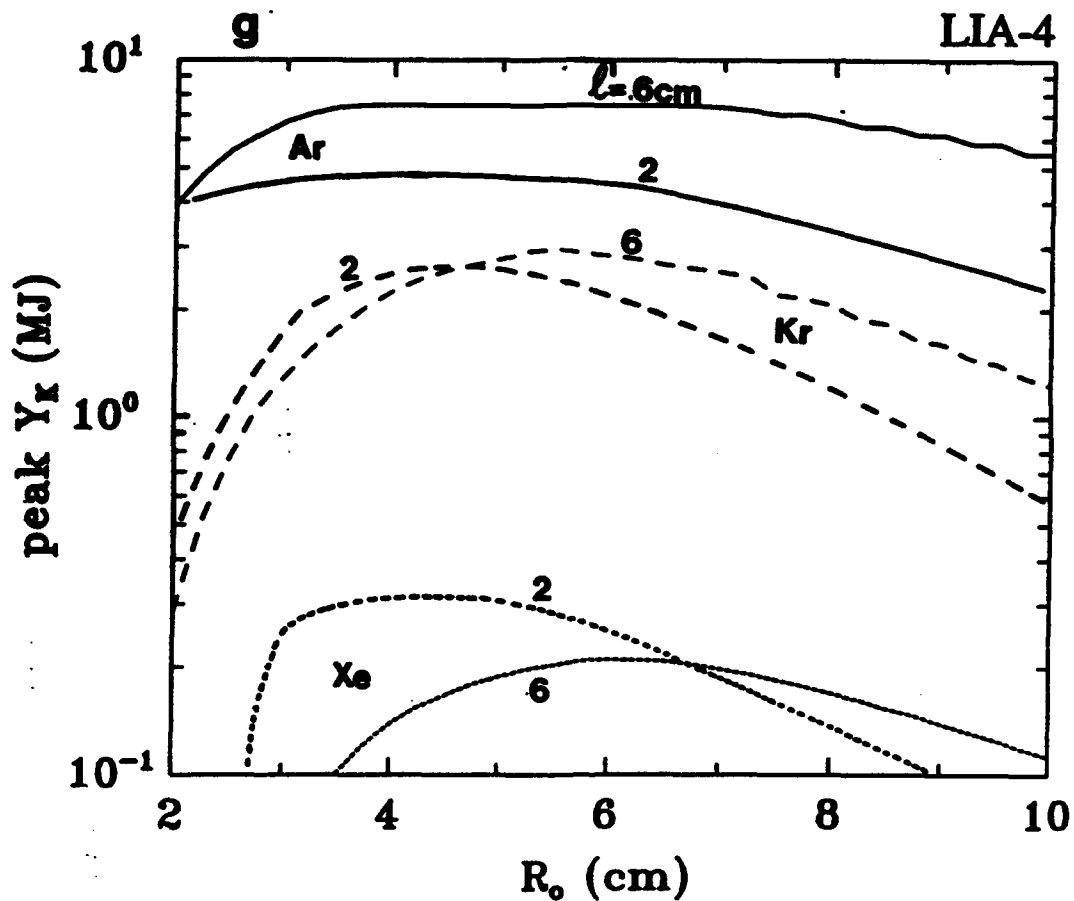
Fig.10(g) A comparison of peak yields as a function of initial radius for a short (2 cm) long pinch and a long (6 cm) one on the LIA-4 design. Yields from low Z material are optimized at large R_o, while yields form high Z material are better from pinches with a short length. (L_f = 1.94 nH).
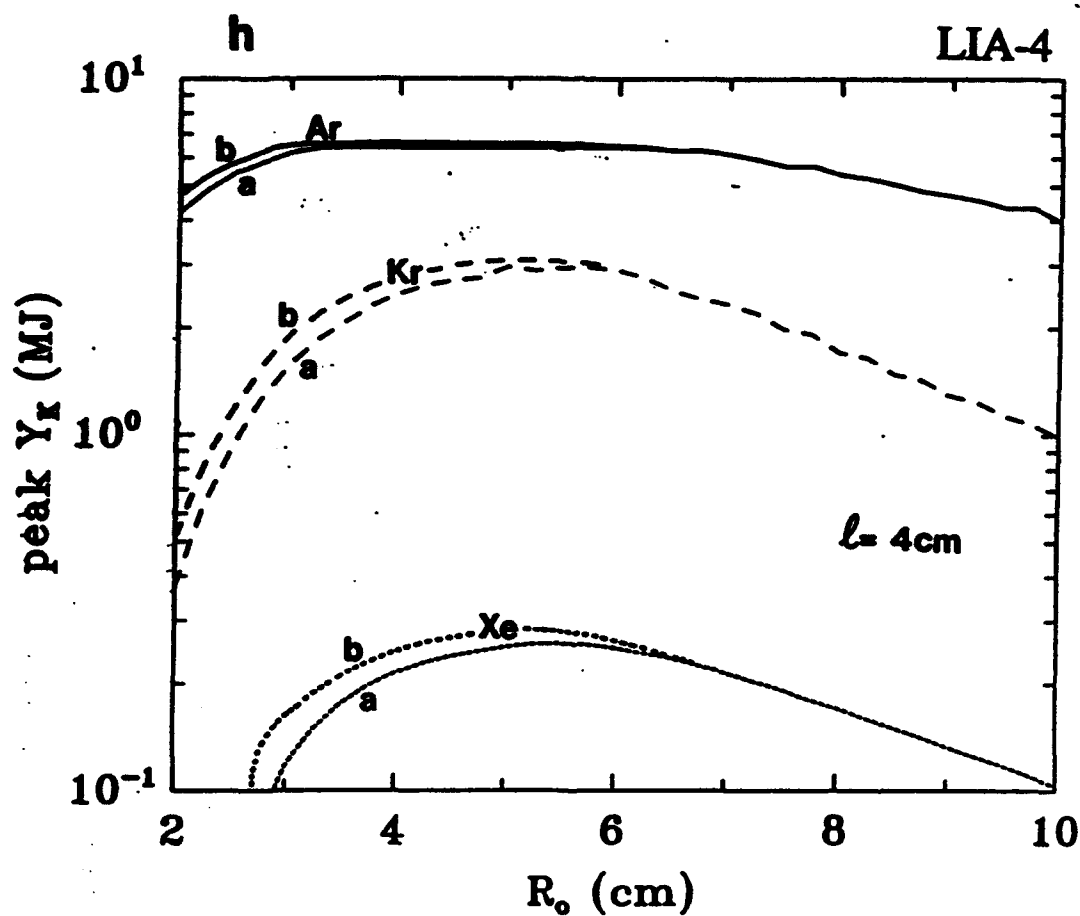
Fig.10(h) Peak K-shell yields on LIA-4 over initial radius for the final feed inductance L_f of 1.94 nH (case a) vs 2.86 nH (case b) from Table I. The yield differences are clearly small, i.e., change in final feed inductance with R_o is negligible, but there is a systematic trend in the LIA of higher yields with large front end inductance.

Table II. Peak K-Shell Yields for LIA-4 from the J-Scaling Law.

|	ℓ (cm)	R_o (cm)	t_{imp} (ns)	M (mg)	E_K (MJ)	$Y_K(Ar)$ (MJ)	$Y_K(Kr)$ (MJ)	$Y_K(Xe)$ (MJ)
LIA-4	6	6.5	120	28	25	7500		
LIA-4	6	3.7	120	86	25	7500		
LIA-4	6	2.0	70	48	14	3900		
LIA-4	4	6.2	115	23	21	6400		
LIA-4	4	3.5	115	68	21	6400		
LIA-4	4	2.0	75	48	14	4200		
LIA-4	2	5.7	110	13	15	4600		
LIA-4	2	3.0	110	48	15	4600		
LIA-4	2	2.0	80	43	13	3900		
LIA-4	6	5.5	110	30	24		3000	
LIA-4	6	4.0	85	23	18		2200	
LIA-4	6	2.0	60	25	10		290	
LIA-4	4	5.0	100	23	20		3000	
LIA-4	4	4.0	85	19	17		2500	
LIA-4	4	2.0	60	25	10		370	
LIA-4	2	4.8	100	15	15		2600	
LIA-4	2	4.0	85	13	14		2500	
LIA-4	2	2.0	70	25	11		420	
LIA-4	6	6.2	110	25	24			210
LIA-4	6	4.0	80	19	17			140
LIA-4	6	2.0	-	-	-			0
LIA-4	4	5.5	105	21	21			260
LIA-4	4	4.0	80	17	16			210
LIA-4	4	2.0	-	-	-			0
LIA-4	2	4.5	95	15	15			315
LIA-4	2	4.0	90	14	14			310
LIA-4	2	2.0	-	-	-			0
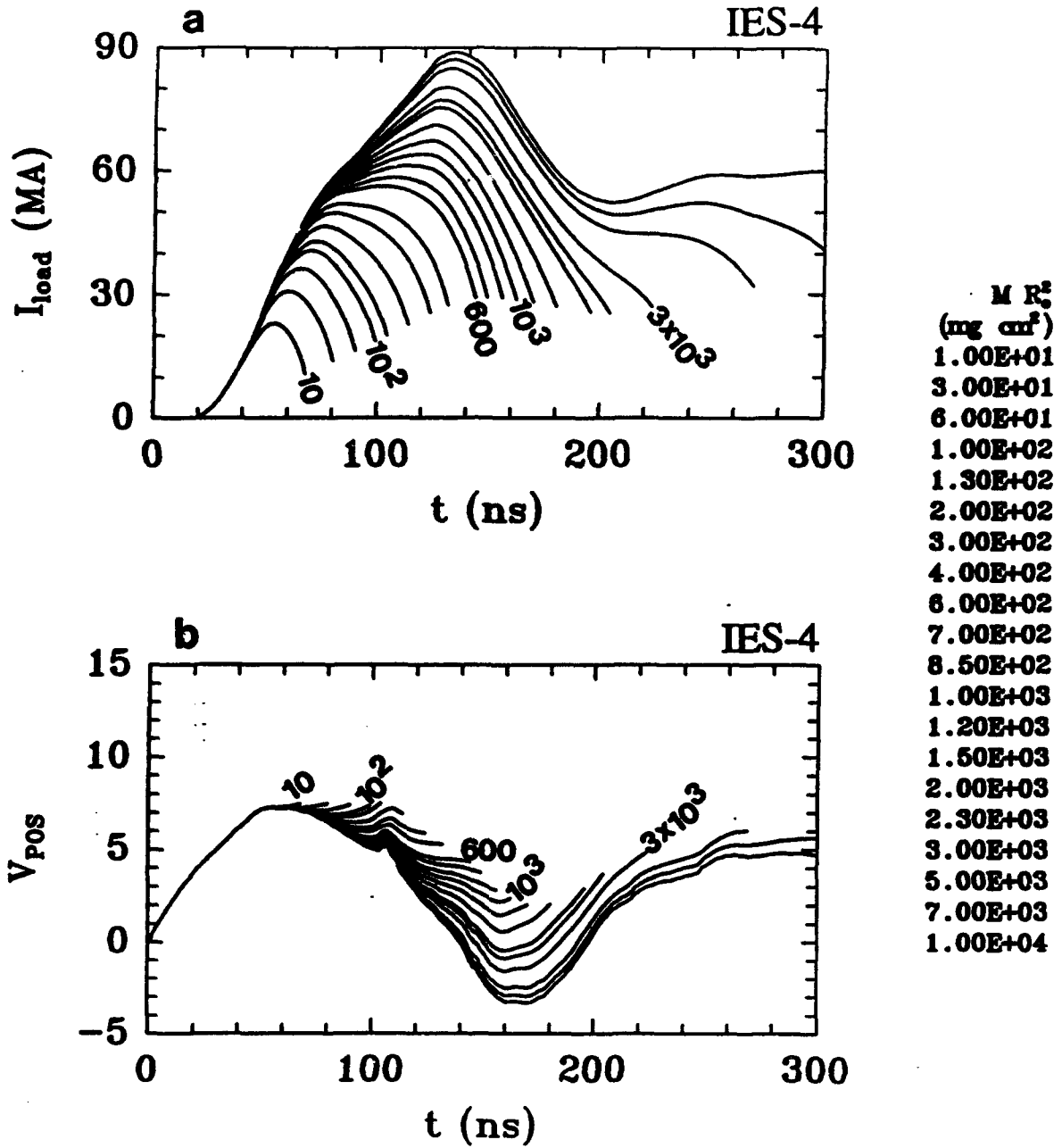
Fig.11(a) The current profiles and coax MITL voltages (b) for IES-4 for various values of MR_o^2. The time $t = 0$ corresponds to the time of POS opening. The pinch length is 4 cm, the final feed inductance $L_f = 1.94$ nH from Table I.
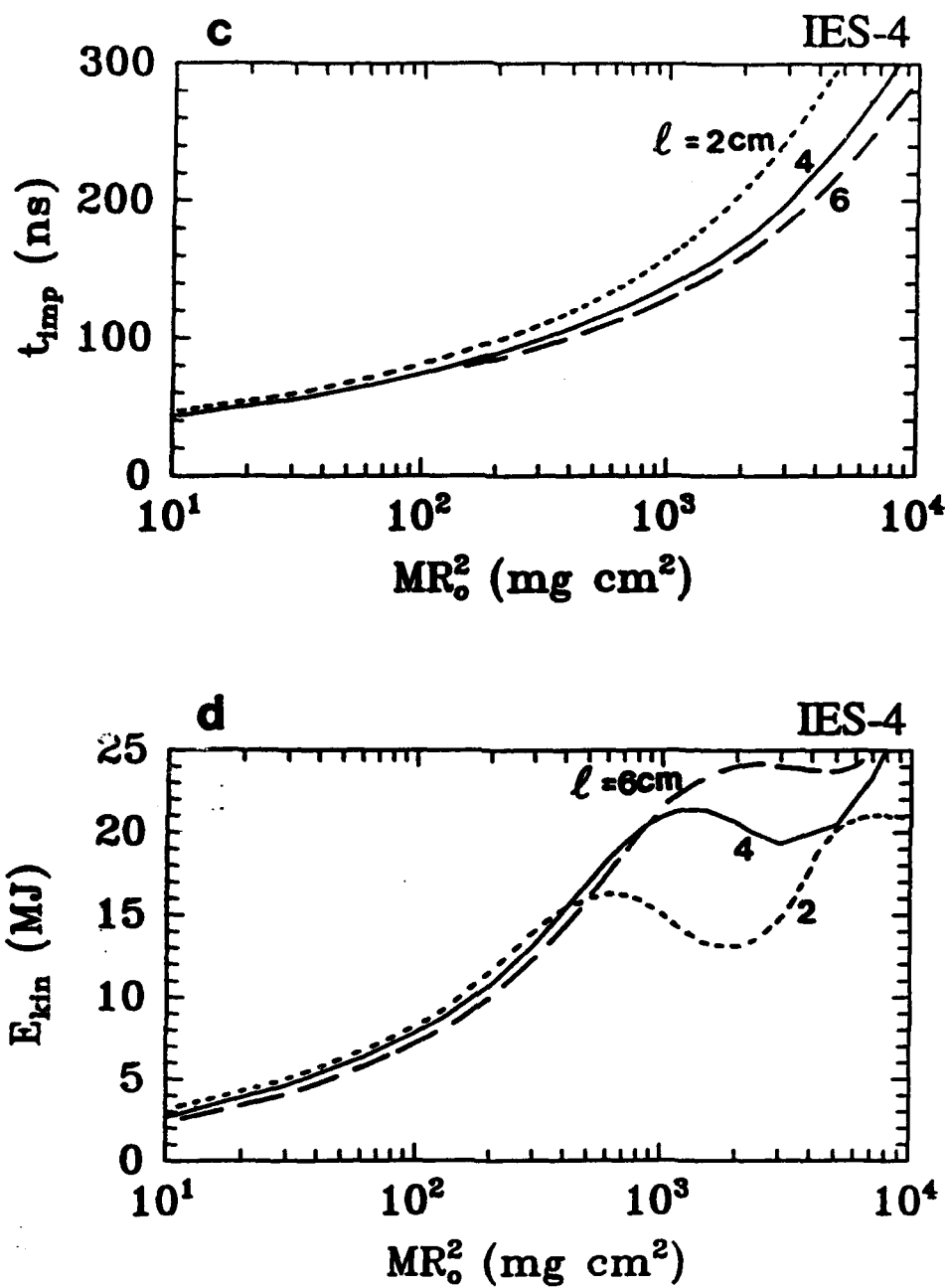
Fig.11(c) The implosion time for three pinch lengths (ℓ) on IES-4 as a function of MR_o^2. **(d)** The plasma kinetic energy at implosion for the same lengths. ($L_f = 1.94$ nH).

Fig.11(e) Contours of total krypton K-shell yield based on the scaling law
for the IES-4. Load conditions are the same as in Fig.11a.
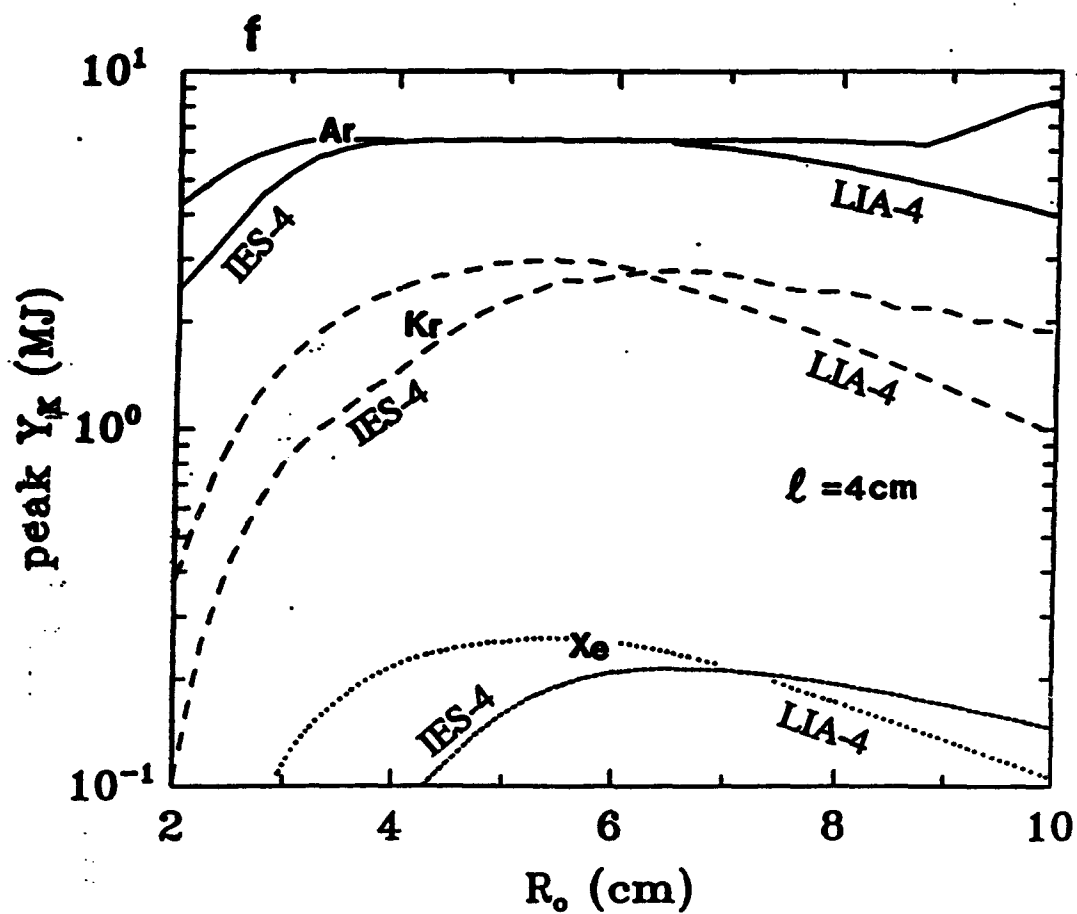
f

Fig.11(f) Peak K-shell yields at different initial radii for Ar(>3 keV), Kr(>13 keV), and Xe($\gtrsim$28 keV) on IES-4. The results for the LIA from Fig.10f are displayed for direct comparison. Load conditions are the same as in Fig.11a.
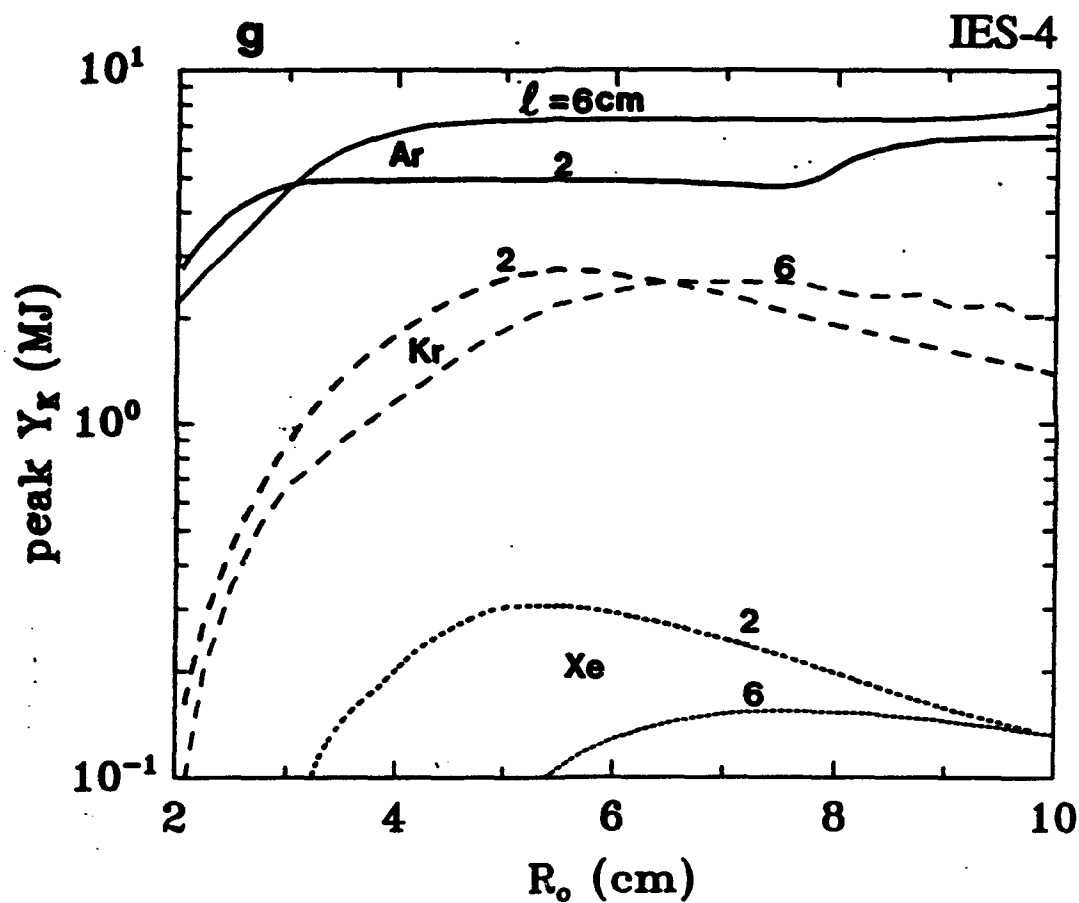
Fig.11(g) A comparison of peak yields as a function of initial radius for a short (2 cm) long pinch and a long (6 cm) on the IES-4 design. Yields from low Z material are optimized at large R_o, while yields form high Z material are better from pinches with a short length. ($L_f = 1.94$ nH).
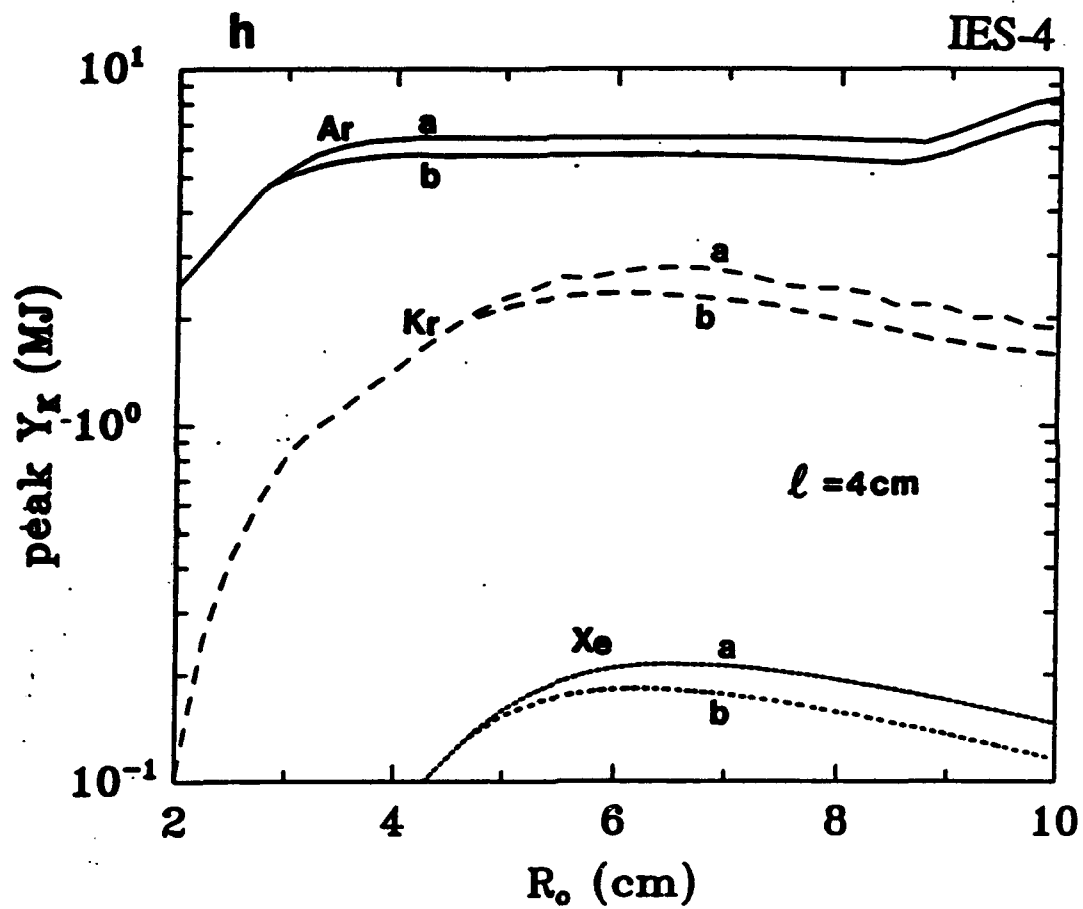
Fig.11(h) Peak K-shell yields on IES-4 over initial radius for the final feed inductance L_f of 1.94 nH (case a) vs 2.86 nH (case b) from Table I. The yield differences are small, i.e., change in final feed inductance with R_o is negligible, but the trend is opposite from the LIA, i.e., smaller front end inductances produce smaller yields at large radii.

Table III. Peak K-Shell Yields for IES-4 from the J-Scaling Law.
(I_{POS} = 90 MA at opening.)

	ℓ (cm)	R_o (cm)	t_{imp} (ns)	M (mg)	E_K (MJ)	Y_K(Ar) (MJ)	Y_K(Kr) (MJ)	Y_K(Xe) (MJ)
IES-4	6	8.5	165	32	24	7300		
IES-4	6	5.2	165	83	24	7300		
IES-4	6	4.0	135	75	22	6700		
IES-4	6	2.0	75	27	8	2200		
IES-4	4	7.5	150	23	21	6400		
IES-4	4	4.2	150	73	21	6400		
IES-4	4	4.0	140	68	21	6300		
IES-4	4	2.0	80	30	8	2500		
IES-4	2	6.2	135	15	16	4800		
IES-4	2	3.3	135	54	16	4800		
IES-4	2	2.0	90	33	9	2700		
IES-4	6	6.5	140	31	23		2500	
IES-4	6	4.0	90	17	12		1200	
IES-4	6	2.0	70	25	7		60	
IES-4	4	6.5	140	26	21		2800	
IES-4	4	4.0	95	16	12		1400	
IES-4	4	2.0	75	25	8		100	
IES-4	2	5.5	125	16	16		2800	
IES-4	2	4.0	95	11	11		1800	
IES-4	2	2.0	80	25	8		130	
IES-4	6	7.5	140	23	23			160
IES-4	6	4.0	80	11	9			43
IES-4	6	2.0	-	-	-			0
IES-4	4	6.5	135	22	21			210
IES-4	4	4.0	90	12	10			80
IES-4	4	2.0	-	-	-			0
IES-4	2	5.2	125	16	16			310
IES-4	2	4.0	100	13	12			210
IES-4	2	2.0	-	-	-			0

VI. Projected K-Shell Yields for Variations of the LIA and IES Designs

The JUPITER circuit designs of Figs.9a and 9b can readily be altered to investigate both the circuit resiliency to front end changes as well as the design flexibility arising from the switch parameters. The nomenclature associated with the different machine versions studied in this section are listed in Table IV.

Table IV. Notes on the Various Machine Versions

nomenclature	description
LIA-4	Fig.9a
LIA-5	twice front end inductance
LIA-6	PFL switch permanently closed
IES-4	Fig.9b
IES-5	twice front end inductance
IES-6	POS opens at 130 MA in storage inductor
IES-7	same as IES-6 but $\Delta t_{open} = 100$ ns, $Z_{flow} = 0.067 \, \Omega$

The front end design, as presently configured with the 4-slot, double post-hole convolute, might be overly aggressive in that the estimated electron losses through this region prove too optimistic. One fallback position would be to return to the original design with a 2-slot, single post-hole convolute. To investigate the effects of this potential course of action upon the projected yields we approximate the latter front end by doubling the impedance of every element starting with the "coax-to-disc convolute" to the "post-hole convolute" element of Figs.9a and 9b. The long MITL in the LIA and the storage inductor in the IES remain unchanged. The 1.94 nH of Table I for $R_o = 5$ cm is replaced by 3.70 nH. The peak yield over R_o for LIA-5 is compared with the previously displayed results for LIA-4 in Fig.12a. Clearly, the adder design is hardly affected by a doubling of the front end inductance. The similar performance for the higher inductance front end is due to a corresponding increase in the MITL voltage of Fig.11b, from a plateau of $\sim$7MV to $\sim$9 MV. The front end of LIA-5 is closer to a matched load since the reflected voltage wave is reduced. A similar insensitivity in the coupled kinetic energy due to moderate changes in the front end inductance was found by Corcoran [Ref.11] when MITL losses were included. On the

44

other hand, the IES-5 system is compromised by an increase in the inductance as shown in Fig.12b. According to Ref.12, any increase in the front end inductance between the storage inductor and the load for an IES system leads to a degradation in energy coupling to the pinching load. For IES-5 the peak Y_K in argon, krypton, and xenon is only about $^2/_3$ of that from IES-4.

It is possible to draw on the inherent flexibility of each design to either lower the magnitude of the driving voltage pulse or tap more energy from the generator. In the LIA suppose the PFL switch is permanently closed. Then one can both gain back energy lost during the resistive closing phase of the switch and lower the peak voltage by stretching out the pulse in time. For the design version LIA-6, the PFL switch of Fig.9a is closed at $t = 0$ and the initial charge on the intermediate store is raised to 16.8 MV to account for the absence of energy dissipation [Ref.13]. The front end returns to the low inductance 4-slot version. Figures 13a and 13b present the load current and MITL voltage for LIA-6 for various MR_o^2, and can be directly compared to the LIA-4 results in Figs.10a and 10b. Because of the absence of power compression via the PFL switch, the current and voltage profiles are significantly elongated compared to LIA-4. For each fixed MR_o^2 the peak current of LIA-6 is lower than in LIA-4, but the same is not true of V_{MITL}. For instance, at $MR_o^2 = 10^3$ mg cm^2 the peak V_{MITL} is ~ 8 MV in both cases, although this peak is attained near the beginning of the pulse in LIA-4 while at implosion in LIA-6. The MITL voltage for $MR_o^2 > 2000$ mg cm^2 is only about half that on LIA-4, which would indicate that electron insulation would be easier to sustain on LIA-6. The implosion times for the same MR_o^2 are significantly longer in LIA-6 than LIA-4 as shown in Fig.13c. Figure 13d shows that the peak coupled kinetic energy for LIA-6 is smaller and shifted to a higher MR_o^2 compared to LIA-4. As we have seen before, this means that the initial radius leading to the peak K-shell yields are also increased, as born out by Fig.13e. As a matter of fact, the Xe yield for LIA-6 does not show up on the graph and for $R_o < 10$ cm the peak yields in Ar, Kr, and Xe are all smaller than the peak Y_K from LIA-4. Table V lists peak yields at several radii and associated t_{imp}, M, and E_K for LIA-6 with $\ell = 4$ cm. The results for LIA-4 are included from Table II for ease in comparison. Clearly, the permanent closure of the PFL switch offers no advantage to the adder in terms of yield, but some advantage of a low V_{MITL} when MR_o^2 is large.

The plasma opening switch in the IES design likewise offers the potential to tap more energy from the generator. In the standard LIA-4 design, the switch begins to open when the current in the storage element reaches 90 MA. In terms of Fig.9b this occurs 0.96 μs after the energy begins to flow out of the marx banks. However, the storage current is till rising as this time and, if the opening of the POS is delayed until 1.33 μs, the current in the storage element peaks out at 130 MA. We will refer to the IES design version with the latter switch opening time as IES-6. As noted above, the actual conduction time of the switch is smaller than 1.33 μs due to the wave transit time

from the marx to the POS. Measured from the time that the POS first begins to carry 1 MA, the effective conduction time for IES-6 is 1.08 μs, compared to 0.7 μs for IES-4. The increase in the load current for IES-6 is demonstrated in Fig.14a where, for instance, the peak current for MR_o^2 = 2000 mg cm^2 is ~85 MA for IES-6, but ~75 MA for IES-4 (see Fig.11a). The time to reach this peak, ~95 ns, is same in both designs because we have kept the same opening time Δt_{open} and Z_{flow} switch parameters. Consequently, the initial peak of the voltage across the POS, shown in Fig.14b, is larger for IES-6 than for IES-4 (Fig.11b). If, instead of maintaining the same switch parameters, it is found that the price of a longer conduction time switch is both a slower opening and a smaller flow impedance, the current and voltage results are quite different. Fig.14c and 14d present I_{load} and V_{POS} for the same long conduction switch but twice the opening time and half the flow impedance. This design version is termed IES-7. Note the peak current for MR_o^2 = 2000 mg cm^2 is only ~70 MA and it takes ~120 ns to reach it. The initial rise of V_{POS} is also reduced below IES-4 and IES-6. The implosion times and kinetic energies for the three version IES-4, -6, and -7 are displayed in Figs.14e and Fig.14f, respectively. The higher currents of IES-6 lead to shorter t_{imp}, and inversely for IES-7. For the E_K coupled to the load, the peak for IES-6 is substantially above that for the standard model but at nearly the same MR_o^2. For IES-7 the peak E_K is also larger, but occurs at a larger MR_o^2. The peak K-shell yield for the three operating versions as a function of initial radius is shown in Fig.14g. As expected, IES-6 offers a substantial increase in the Ar, Kr, and Xe yields, and yields near the peak can be obtained at smaller radii on IES-6 than on IES-4 and IES-7. However, if the long conduction switch does not open in a similar manner to that of the standard case, but instead the opening parameters become degraded, as for IES-7, then the radii required to reach the same peak as in IES-4 move significantly outward. Table VI lists peak yields at several radii and associated t_{imp}, M, and E_K for IES-6 and IES-7 with ℓ = 4 cm. The results for IES-4 are included from Table III for ease in comparison. In summary, the advantages offered by a longer conduction time in the IES design can only be realized if (i) insulation can be maintained at ~10 MV and (ii) the switch performance in terms of opening time and flow impedance are not seriously degraded.
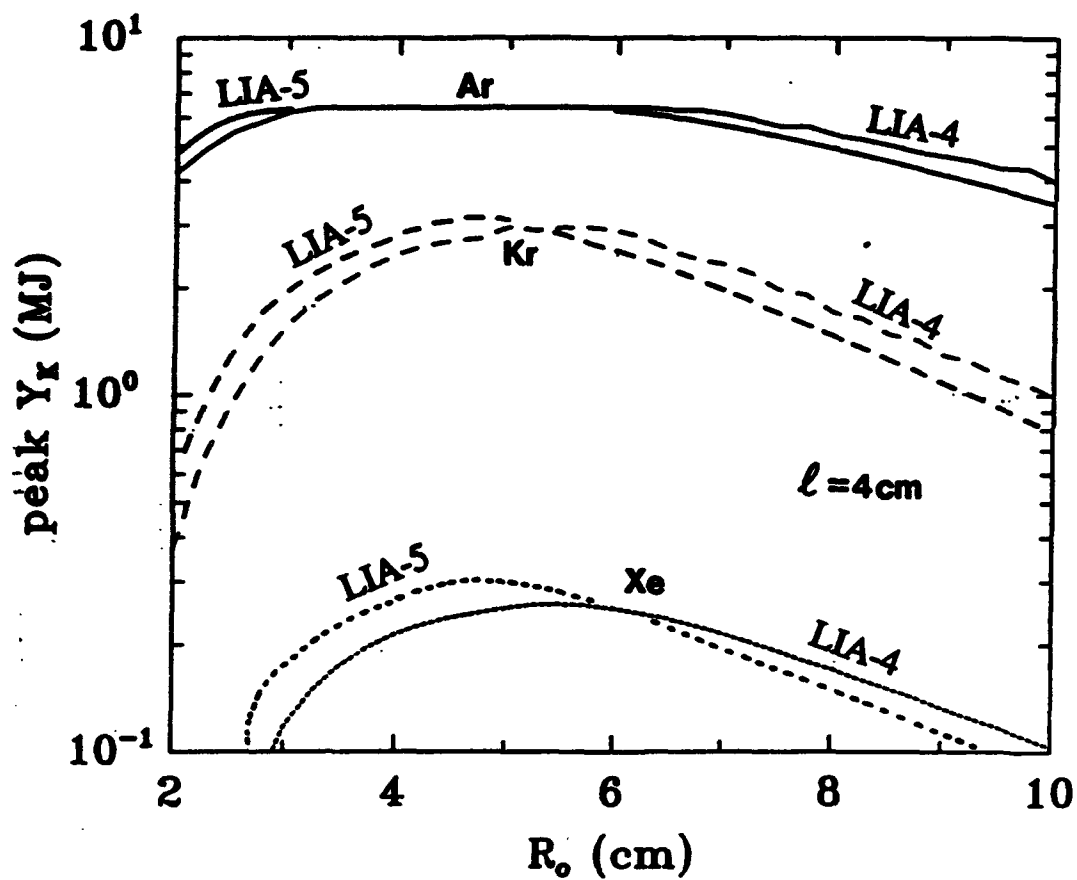
Fig.12(a) Comparison of the peak yields over initial radius for the standard (LIA-4) and high inductance front end (LIA-5) versions of the adder designs. There is negligible difference between them. ($L_f = 1.94$ nH.)
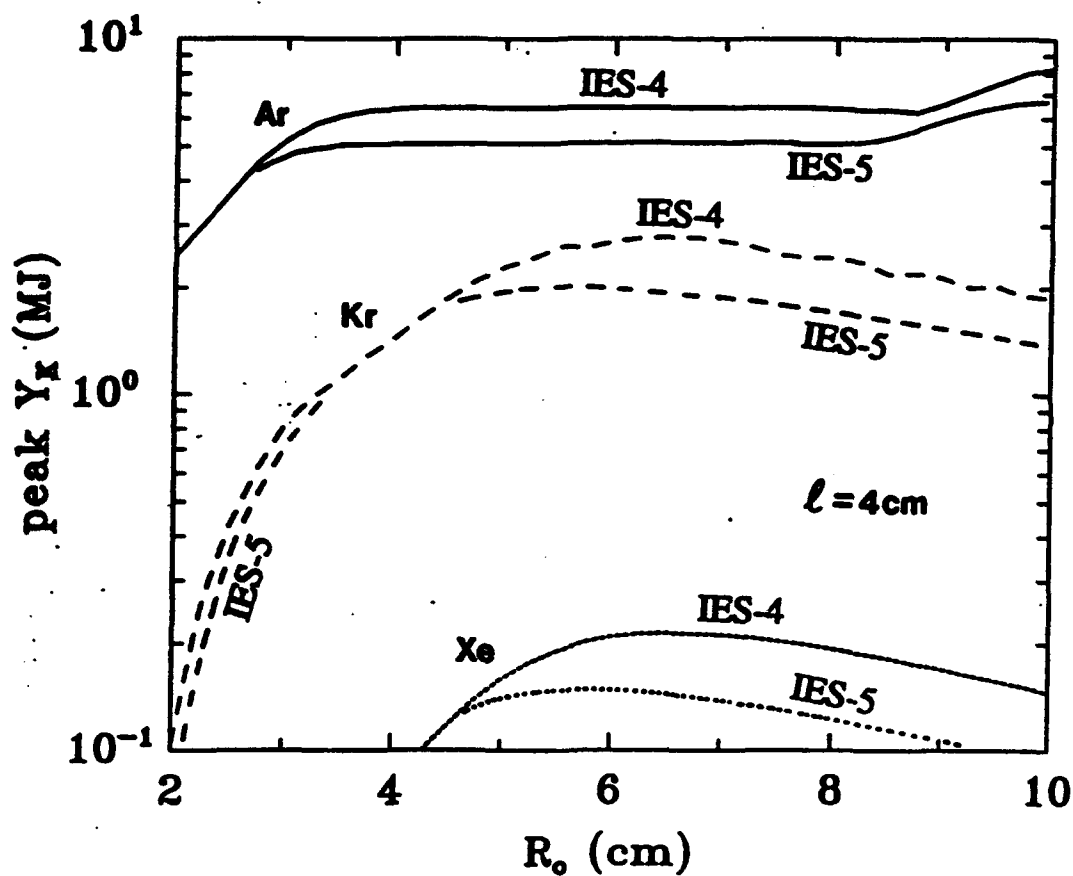
Fig.12(b) Comparison of the peak yields over initial radius for the standard (IES-4) and high inductance front end (IES-5) versions of the inductor designs. The peak Y_K for IES-5 is $\sim$ $2/3$ of IES-4. ($L_f = 1.94$ nH.)
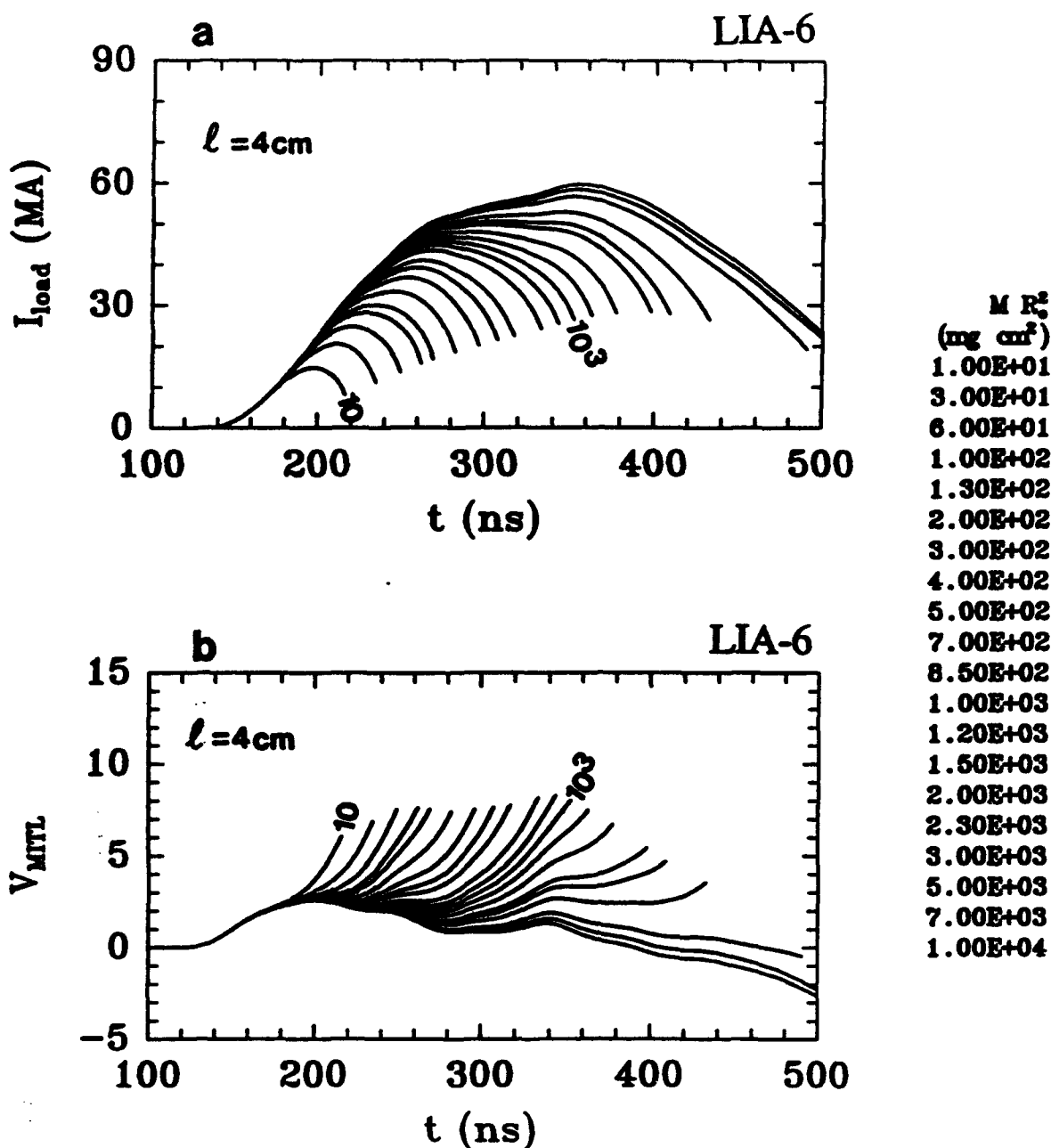
Fig.13(a) Load current and MITL voltage (b) profiles for the adder design
version with a permanently closed PFL switch, i.e., LIA-6. Broader profiles
and lower peak currents can be seen by comparison with LIA-4 in Figs.10a
and 10b. (L_f = 1.94 nH.)
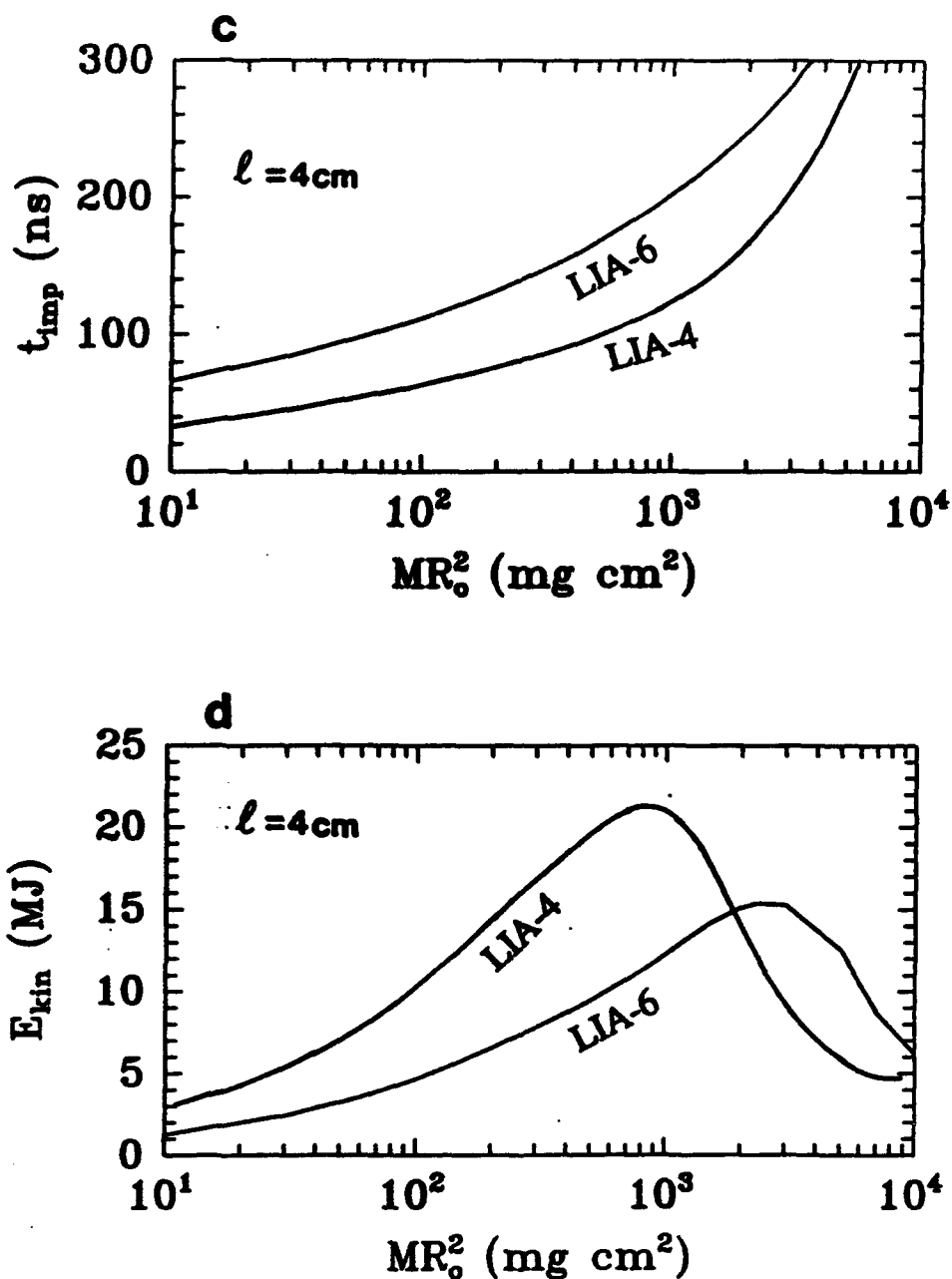
Fig.13(c) Comparison of implosion times and coupled kinetic energies (d) for LIA-4 and LIA-6. The broad profiles of Fig.13a and 13b lead longer t_{imp}, smaller E_K, and a shift in the peak kinetic energy over MR_o^2 compared to LIA-4. ($L_f = 1.94$ nH.)

Fig.13(e) Comparison of the peak K-shell yields in Ar, Kr, and Xe for LIA-6 and LIA-4. The Xe yield form LIA-6 is below 100 kJ. The shift in E_K vs MR_o^2 causes the radius for peak yield to increase. ($L_f = 1.94$ nH.)

Table V. Peak K-Shell Yields for Two LIA Versions

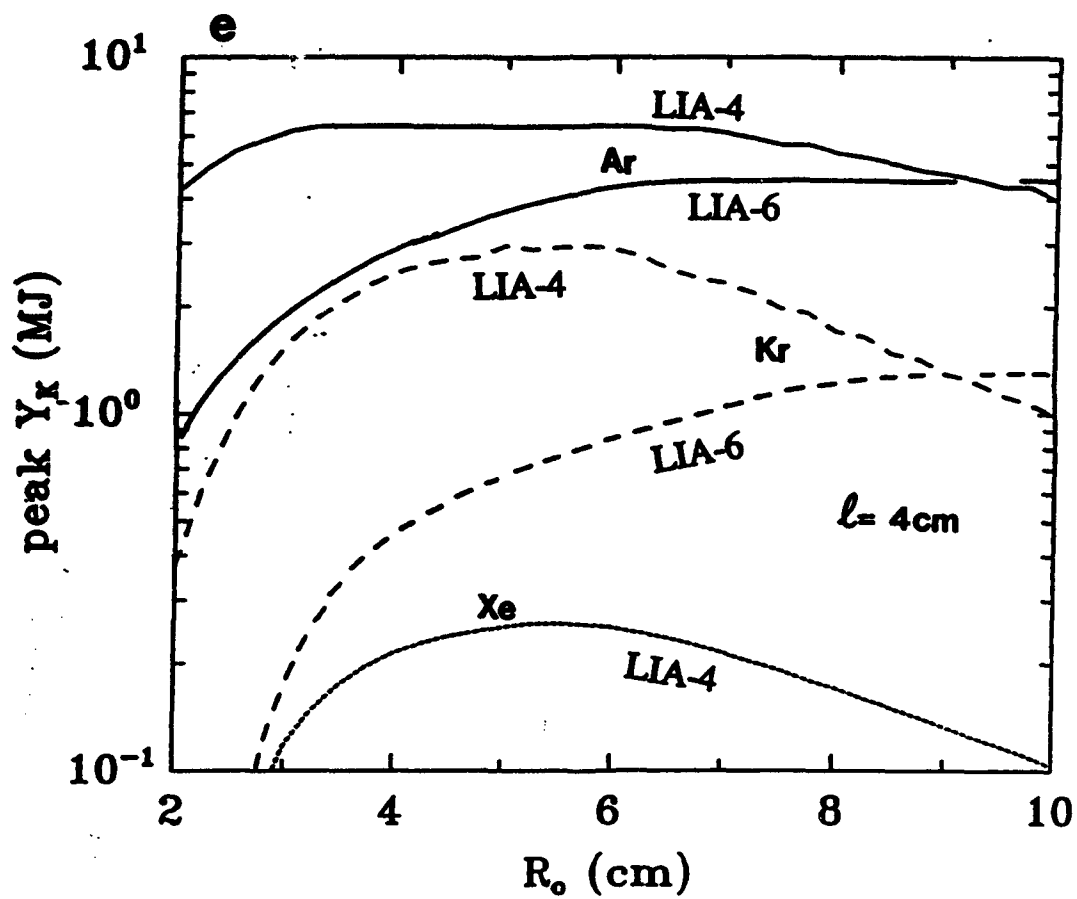|	ℓ (cm)	R_o (cm)	t_{imp} (ns)	M (mg)	E_K (MJ)	Y_K(Ar) (MJ)	Y_K(Kr) (MJ)	Y_K(Xe) (MJ)
LIA-4	4	6.2	115	23	21	6400		
LIA-4	4	3.5	115	68	21	6400		
LIA-4	4	2.0	75	48	14	4200		
LIA-6	4	7.0	265	51	15	4600		
LIA-6	4	4.0	170	33	10	2900		
LIA-6	4	2.0	110	25	5	810		
LIA-4	4	5.0	100	23	20		3000	
LIA-4	4	4.0	85	19	17		2500	
LIA-4	4	2.0	60	25	10		370	
LIA-6	4	8.8	240	23	15		1400	
LIA-6	4	4.0	125	10	6		470	
LIA-6	4	2.0	-	-	-		0	
LIA-4	4	5.5	105	21	21			260
LIA-4	4	4.0	80	17	16			210
LIA-4	4	2.0	-	-	-			0
LIA-6	4	10.0	225	14	14			650
LIA-6	4	4.0	110	6	5			85
LIA-6	4	2.0	-	-	-			0

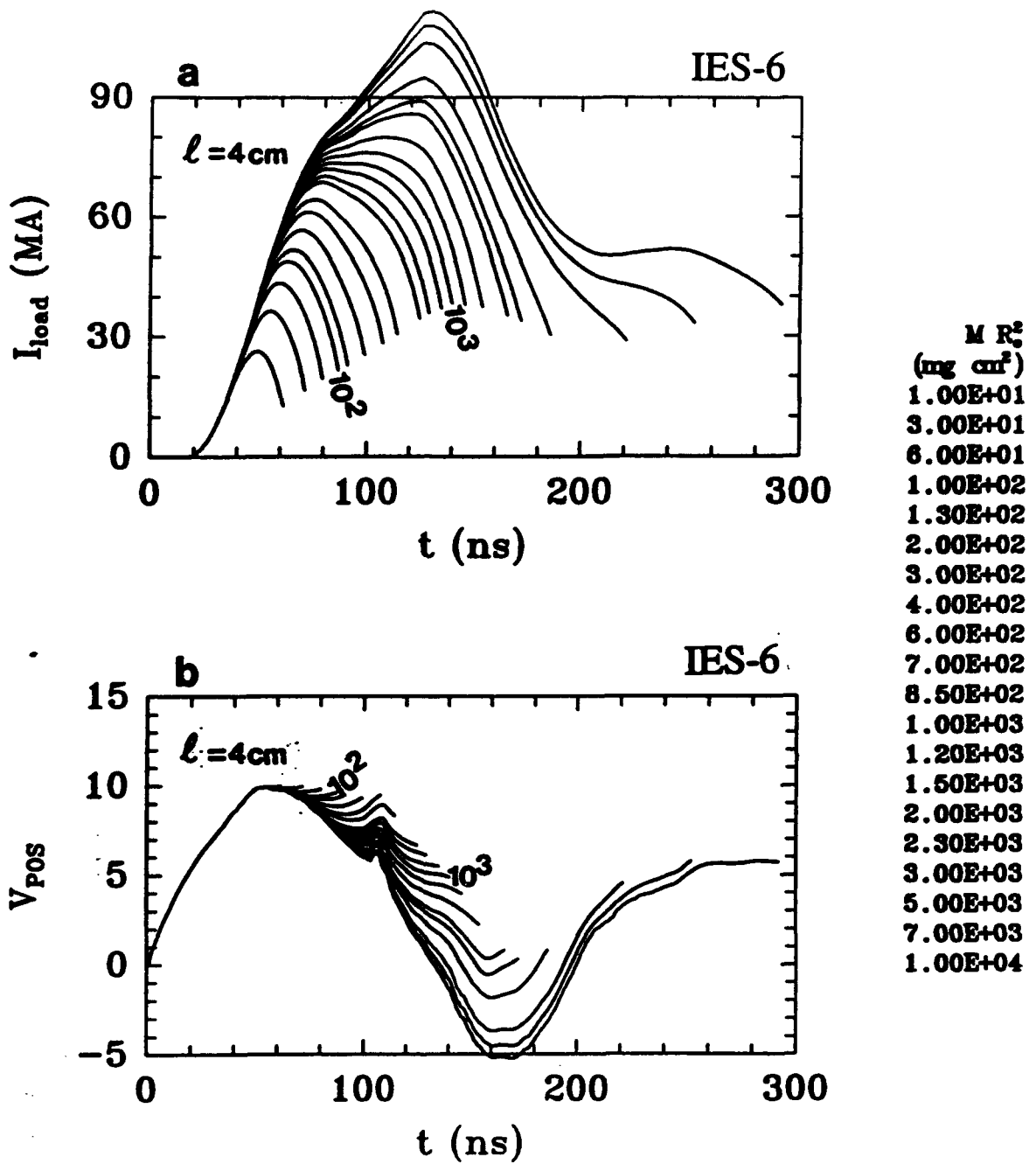|	M R²c
	(mg cm²)
	1.00E+01
	3.00E+01
	6.00E+01
	1.00E+02
	1.30E+02
	2.00E+02
	3.00E+02
	4.00E+02
	6.00E+02
	7.00E+02
	8.50E+02
	1.00E+03
	1.20E+03
	1.50E+03
	2.00E+03
	2.30E+03
	3.00E+03
	5.00E+03
	7.00E+03
	1.00E+04

Fig.14(a) Load current and MITL voltage (b) profiles for IES-6. The conduction time of this design version opens with 130 MA in the storage inductor, as opposed to 90 MA for the standard IES-4. The opening time and Z_{flow} are the same as IES-4. Note the enhanced load current, but also the larger V_{POS}, compared to the standard version in Figs.11a and 11b. (L_f = 1.94 nH.)
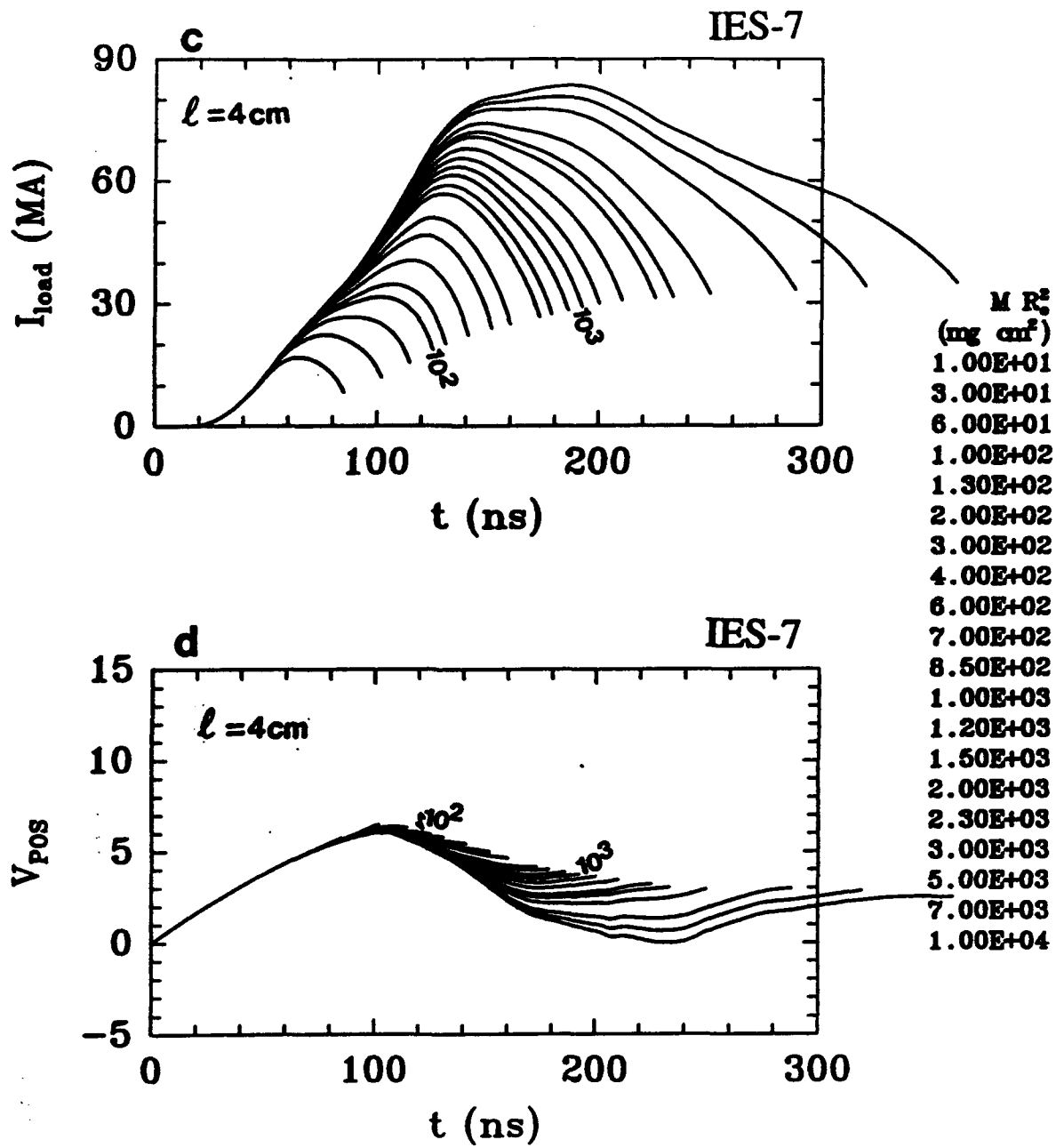
Fig.14(c) Load current and MTTL voltage (d) profiles for IES-7. As for IES-6, the conduction time of this design version also opens with 130 MA in the storage inductor, but the opening time is doubled and Z_{flow} halved compared to IES-4 and IES-6. Consequently both I_{load} and V_{POS} are reduced and stretched. (L_f = 1.94 nH.)
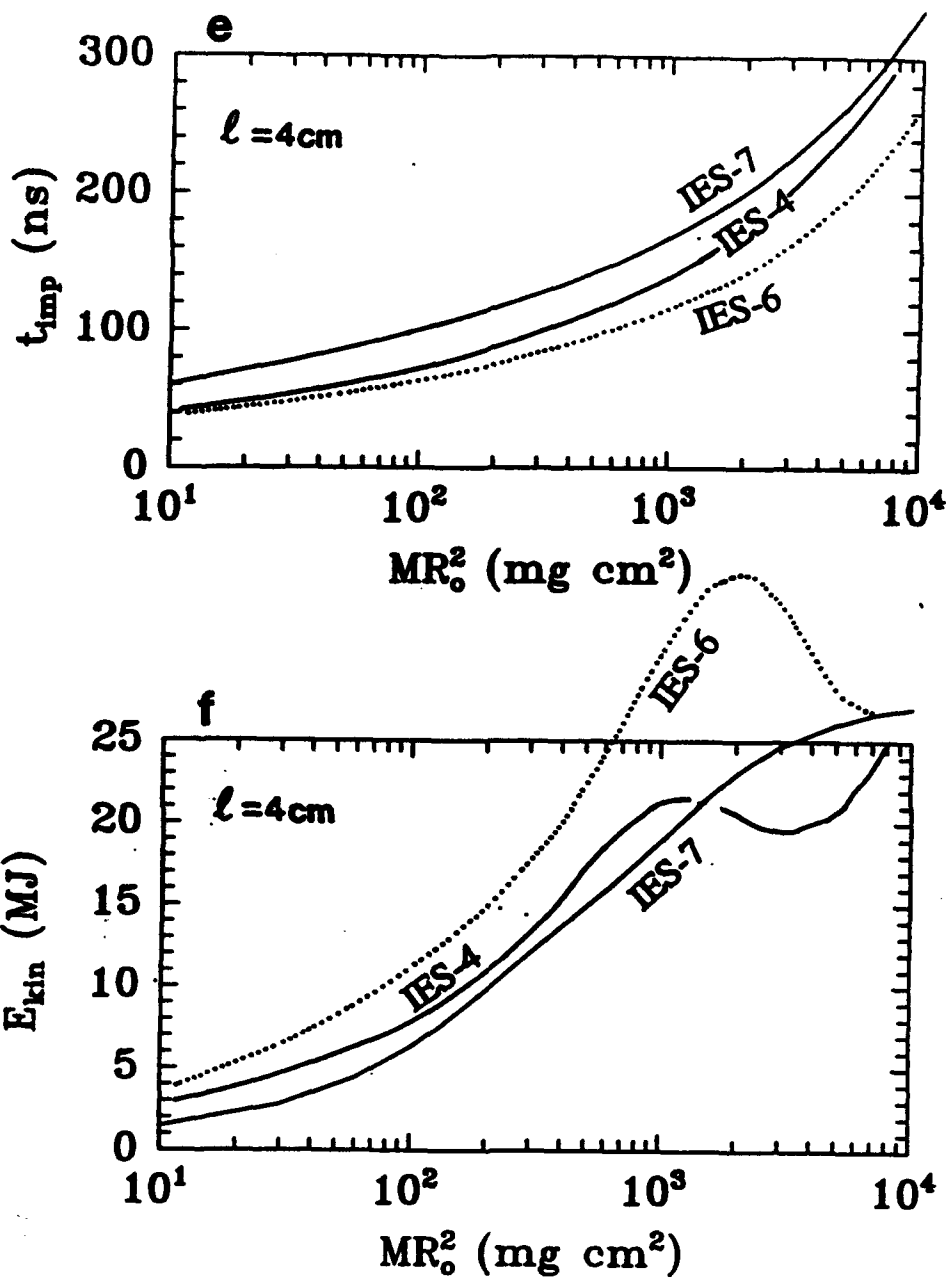
Fig.14(e) Comparison of implosion times and coupled kinetic energies (f) for IES-4, IES-6, and IES-7. ($L_f = 1.94$ nH.)

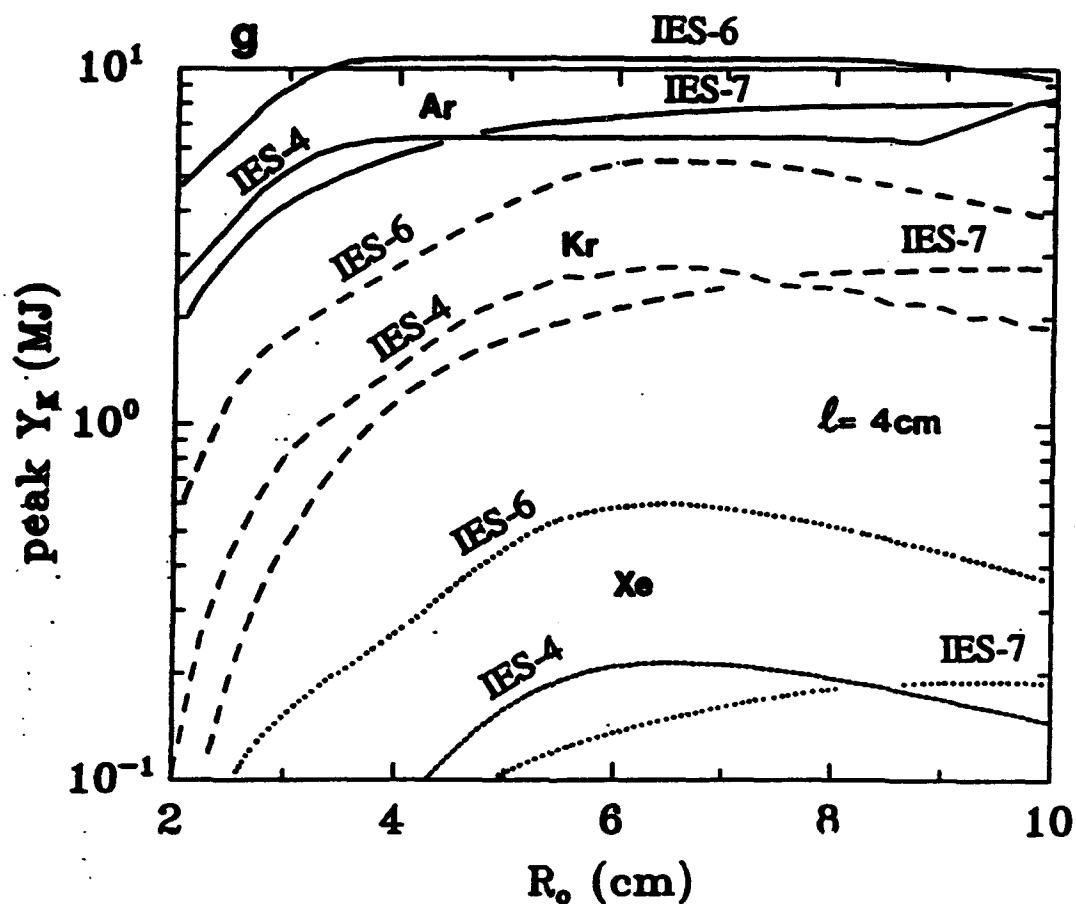**Fig.14(g)** Comparison of the peak K-shell yields in Ar, Kr, and Xe for IES-4, IES-6, and IES-7. Note that if the POS in the long conduction version opens in a similar manner as in the standard version (IES-4) then the yields (IES-6) are significantly improved. However, if the long conduction time seriously deteriorates the POS opening (IES-7), then the yield performance is not enhanced for Kr and Xe. ($L_f = 1.94$ nH.)

Table VI. Peak K-Shell Yields for Three IES Versions

	ℓ (cm)	R_o (cm)	t_{imp} (ns)	M (mg)	E_K (MJ)	$Y_K(\mathrm{Ar})$ (MJ)	$Y_K(\mathrm{Kr})$ (MJ)	$Y_K(\mathrm{Xe})$ (MJ)
IES-4	4	7.5	150	23	21	6400		
IES-4	4	4.0	140	68	21	63 00		
IES-4	4	2.0	80	30	8	2500		
IES-6	4	8.0	140	33	35	10600		
IES-6	4	4.0	140	119	35	10600		
IES-6	4	2.0	75	52	15	4500		
IES-7	4	10.0	325	91	27	8100		
IES-7	4	4.0	170	68	20	5700		
IES-7	4	2.0	115	48	9	1800		
IES-4	4	6.5	140	26	21		2800	
IES-4	4	4.0	95	16	12		1400	
IES-4	4	2.0	75	25	8		100	
IES-6	4	6.2	125	34	33		5500	
IES-6	4	4.0	85	21	19		2700	
IES-6	4	2.0	62	25	11		500	
IES-7	4	9.2	220	32	24		2800	
IES-7	4	4.0	120	14	10		1200	
IES-7	4	2.0	-	-	-		0	
IES-4	4	6.5	135	22	21			210
IES-4	4	4.0	90	12	10			80
IES-4	4	2.0	-	-	-			0
IES-6	4	6.5	130	34	34			600
IES-6	4	4.0	85	21	19			260
IES-6	4	2.0	-	-	-			0
IES-7	4	9.5	205	23	23			190
IES-7	4	4.0	115	11	9			50
IES-7	4	2.0	-	-	-			0

VII. Summary and Conclusions

The objective of the present investigation was to estimate radiation yields from JUPITER-class generators based on scaling laws. Because z-pinches on JUPITER may not implode to as small a radius as seen on DOUBLE EAGLE and SATURN, and because some JUPITER loads will consist of high atomic number material, two revisions to the established scaling law of Whitney, et al., [Ref.2] and Thornhill, et al. [Ref.3] were necessitated. First, a dependency on the final pinch radius R_f was incorporated to account for the pinch density ($\propto R_f^2$). This is relevant in the optically thin radiation limit. Second, a multiplicative factor ϵ_L derived from Fig.1 was used to account for implosions which are barely energetic enough to ionize the pinch material into the K-shell stage. In the parlance of eqn.(1), these implosions have $\eta \lesssim 1$. These revisions are included in the J-scaling law of eqns.(3), (4), and (5). In the efficient regime [eqn.(3b)] the K-shell yield is $\sim30\%$ of the coupled kinetic energy E_K. The transition from this regime to the inefficient regime [eqn.(3a)] occurs at the mass breakpoint M_{BP} given in eqn.(7). Theoretical predictions for the yield emerge from a combination of a thin shell model for the implosion dynamics, a circuit for the generator, and the K-shell radiation J-scaling law. In the present approach, given a machine circuit, pinch length ℓ, initial load inductance L_w, and an assumed compression ratio R_f/R_o, the implosion time t_{imp} and coupled load kinetic energy E_K are dependent only on the product $M R_o^2$.

To assess the accuracy of the revised J-scaling law, predictions for the K-shell yield of aluminum on DOUBLE EAGLE and SATURN were compared with experimental data in the load mass – initial radius ($M - R_o$) plane of Figs.6a and 6b, respectively. A compression factor R_f/R_o of $1/7$ was assumed. The predictions of peak yields agree with the data for SATURN, but underestimated the DOUBLE EAGLE data. The latter data suggest that DOUBLE EAGLE can achieve nearly 100% conversion of kinetic energy into K-shell radiation, much larger than the $\sim30\%$ conversion efficiency found from the simulations used to derive the scaling law. The J-scaling law is based only on the thermalization of kinetic energy and does not include resistive heating in the pinched phase. Thus this law can be employed as a conservative predictor for yields on JUPITER-class generators, assuming that both the thermalization dynamics and the atomic number Z dependence derived for the scaling relations also apply to krypton and xenon on JUPITER.

In applying the J-scaling relations to JUPITER-class generators two approaches were taken. The first was to use an equivalent Thevenin circuit (Fig. 7) to model a general machine capable of producing 10 to 100 MA load current. Fig.8 shows that low Z material, such as aluminum ($Z = 13$) and argon ($Z = 18$), will radiate in the efficient I^2 regime, i.e., $Y_K \sim 0.3 E_K$, on JUPITER. On the other hand, radiation from high Z material like xenon ($Z = 54$) varies as I^4, which indicates the inefficient regime. Krypton ($Z = 36$) would be in the efficient regime if the peak load current were

~100 MA. At the anticipated JUPITER current level of ~60 MA, krypton is a transition radiator between the two regimes.

The second approach was to look at specific candidate designs for JUPITER and assess their individual radiation performance. The transmission line circuit used to model the 4 cells/module, 30 module Linear Inductive Adder (LIA-4) with a low inductance, 4-slot front end is presented in Fig.9a. Figure 9b shows the transmission line circuit used for the 60 module Inductive Energy Store (IES) design with a similar low inductance, 4-slot front end. Many assumptions, listed at the beginning of Section V, were incorporated into the circuit modeling of these machines. One of these involved the use of a constant final feed inductance L_f independent of the initial radius. This simplification facilitated the calculation of yields for many different initial masses M and radii R_o. Variations of the final feed inductance with R_o and ℓ were presented in Table I. The dependence of the load inductance on pinch length ℓ was always accounted for in the calculations. To predict the yields the circuits were combined with a thin shell model for the pinch dynamics and the J-scaling law for the K-shell radiation output. For both machines the compression factor R_f/R_o was fixed at $1/10$. Smaller compressions lead to correspondingly smaller yields, but the trends similar. Four main results emerged from the study of these two standard JUPITER candidate designs:

- For values of MR_o^2 which lead to optimal E_K coupling, the voltages both at the long MITL in LIA-4 and across the switch in IES-4 reach a plateau at about 7 MV (Fig.10b and 11b). However, this occurs ~35 ns after the initial voltage rise on the former design and ~50 ns on the latter. Consequently, the load current (I_{load}) risetime is longer on IES-4 than LIA-4: I_{load} reaches its peak of 71 MA at 70 ns for $MR_o^2 = 10^3$ mg cm^2 and $\ell = 4$ cm on LIA-4, while for the same the conditions the peak I_{load} is 65 MA at 100 ns on IES-4.

- The peak value of E_K for pinch lengths $\ell = 2, 4,$ and 6 cm are similar for IES-4 and LIA-4, namely ~15, ~21, and ~25 MJ, respectively. However, the initial load configuration leading to the peak E_K are different (Fig.10d and 11d). The peak E_K occurs at MR_o^2/ℓ ~200 mg cm for LIA-4, and ~300 mg cm for IES-4.

- For both machines the total kinetic energy coupled to the load increases with length, but shorter pinches produce more kinetic energy per unit length. This feature impacts the optimal yielding pinch length for different atomic number loads. For low Z material like argon, which are in the efficient regime with $Y_K \sim 0.3E_K$, optimal yields are obtained with long pinches such as 6 cm. On the other hand, for high Z material such as xenon, short pinch lengths ($\ell \sim 2$ cm) produce higher yields. Krypton is in between with 2, 4, and 6 cm giving about the same results (Figs.10g and 11g).

ranging between 4.5 and 7 cm for both machines (Tables II and III).

- The standard circuits with 4 cm long loads produce about the same peak yields for Ar ($\sim$7 MJ), Kr ($\sim$3 MJ), and Xe ($\sim$0.3 MJ) and the initial radii for these yields range from 4.5 to 8.5 cm (Table II and III). However, the variation of Y_K with R_o within each design is different – the peak Y_K for Kr and Xe occurs at a larger radius on IES-4 than on LIA-4 (Fig.11f). Furthermore, the Kr and Xe yields on LIA-4 are superior to those on IES-4 if one restricts the initial radius to $\leq$4 cm . This reflects the differences in voltage and load current risetimes referred to above. One potential advantage of achieving good yields with smaller initial radii lies in limiting the disruption of a thin plasma shell by Rayleigh-Taylor instabilities during the run-in phase. On the other hand, if alternative load designs can mitigate the disruption without loss in yield performance, then smaller R_o are not crucial. More will be discussed on this topic at the end of the present section.

Several versions in both the LIA and IES standard design were investigated to determine the yield response to front end changes and to alternative switch operations. A description of the specific designs and the subordinate versions is presented in Table IV. Three further conclusions were drawn from this study of alternative generator operating points:

- Most of the calculations presented in this paper were performed with a fixed final feed inductance L_f [eqn.(15)] which neglects the dependency of L_f on R_o. A test of this simplification using extreme values for L_f shows that the yields vary slightly (Figs.10h and 11h). However, larger changes to the front end inductance might arise if it is found that the 4-slot, double post-hole convolute design does not adequately maintain insulation of the vacuum electron flow. If the front end design returns to the 2-slot post-hole convolute, then the total inductance of the front end approximately doubles. In the case of the LIA the machine is quite resilient to such changes in the front end (Fig.12a), however the yields for the IES decrease by about $^2/_3$ when the front end inductance is doubled (Fig.12b). The response of a design to various front end inductances should be included when judging the versatility of the adder and inductive store JUPITER designs.

- If the PFL switch on the LIA (see Fig.9a) is permanently closed, then the voltage stress on the MITL is significantly reduced (Fig.13b). The peak E_K is reduced for this LIA-6 version and is shifted to a higher MR_o^2 (Fig.13d). The peak yields are also significantly reduced, and require larger R_o compared to the standard LIA-4 (Fig.13e and Table V). Since the adder concept is basically a voltage driver as far as the load is concerned, any power decompression in the line also reduces energy delivered to the load.

60

- In the standard IES-4 version the POS begins to open when the current in the storage inductor reaches 90 MA. This corresponds to a ∼0.7 μs conduction time on the switch. In the IES-6 and IES-7 versions the conduction time was increased to ∼1.08 μs, when the storage current peaks at 130 MA. For IES-6, the opening time Δt_{open} and Z_{flow} of the switch are the same as for IES-4. There is an significant enhancement of E_K for IES-6 compared to that for IES-4 at the same MR_o^2 (Fig.14f). For the Ar, Kr, and Xe yields, IES-6 provides the largest yields of all the machines studied for any initial radii (Fig.14g and Table VI.). In particular, the peak yields at initial radii $\leq$ 4 cm are larger than those from the standard adder design LIA-4. The long conduction switch clearly gives an advantage to the inductive store design. But it is only a potential advantage. In order for the POS to open fully and quickly as in IES-6, the switch must sustain ∼10 MV (Fig.14b). However, the opening efficiency of a long conduction POS may degrade due to the higher densities needed for longer conduction times. Suppose that a long conduction POS leads to a doubling of the opening time and a halving of Z_{flow}, as modeled in IES-7. Then the Kr and Xe yields will be inferior to those from IES-4 at middle radii (Fig.14g) – one must move out to R_o ∼ 10 cm to achieve similar peak yields as on IES-4. Clearly the physical model for and the operation of the POS must be ascertained to effectively judge any claimed flexibility of the inductive store designs.

In comparing the various JUPITER designs for yield performance within this report, scaling laws were the tool of choice due to the time constraints imposed by the JDOST. Whatever approximations and assumptions are inherent to the J-scaling model, all machines were compared with the same law and the above conclusions were drawn from the trends displayed by the results. These comparisons have been broad in parameter space, but the in-depth analysis of load physics issues relevant to a JUPITER-class generator have been limited. The present J-scaling model is subject to many assumptions and extrapolations. For instance, the employed J-scaling law neglects additional resistive heating during stagnation, neglects the effects of the L- and M-shell atomic physics on the K-shell dynamics as one scales from aluminum up to xenon, and ignores questions regarding the early breakdown and stability of large diameter loads. These aspects lead us to focus on future theoretical research directions which impact JUPITER load designs.

- In an actual implosion the plasma has a spatial distribution in density, temperature, velocity, etc. Though an average velocity may lead to η ∼ 1, a fraction of the plasma along the axis may be heated sufficiently to emit K-shell emission, resistive heating of pinched plasma may also contribute to this emission, and an outer cool region may act to downshift the radiation spectrum. In the initial papers on scaling [Refs.2 and 3] these, and other, effects were accounted for by using multi-zone, numerical simulations to model the dynamics and

radiation production. However, only aluminum implosions were analyzed, and these effects in higher Z elements will be much more severe. The J-scaling law results suggest particular regions of parameter space to focus on with more detailed multi-zone simulation work. The latter should be used to specifically address the larger, longer, and heavier loads of JUPITER. This will help to clarify the potentially unique pinch *stagnation physics* at ~60 MA load current. In conjunction with this approach, the energy coupling between the generator and the load should address the losses due to transition electrons in the MITLs.

- Predictions of aluminum and argon K-shell yields on JUPITER-class generators are reliable because, for a ~60 MA driver, appropriate mass loadings of these materials can be found such that the pinch emits in the efficient regime. In this case, the yield is directly proportional to the coupled kinetic energy, and the calculation of the latter quantity is straightforward. For krypton, the optimal yielding implosions on JUPITER will have $\eta \sim 1$. For xenon, η will be even smaller. In this low η regime, the K-shell yields depend on complex details of the implosions, like kinetic energy thermalization and temperature equilibration, as well as the gross L-shell and M-shell radiation losses during the run-in phase. The response of the dynamics due to these losses from high Z material will be significantly different from the aluminum response, which was used to develop the scaling law. For the high Z material at and above krypton, *ionization dynamics* should be an integral part of rigorous calculations for the high energy photon yields on JUPITER, independent of the mechanism in which one plans to produce the energetic photons.

- For both the LIA and the IES machine in their standard version, the optimal yields arise for R_o between 4.5 and 8.5 cm. The latter value is much larger than present day load configurations. According to Ref.12 the number of Rayleigh-Taylor growth cycles in the linear regime is proportional to $\sqrt{R_o}$. This would suggest that larger diameter loads are more prone to disruption during the run-in phase. A heuristic non-linear treatment of the instability for thin shells is presented by Hussey, et al. [Ref.5]. But at present it remains unclear to what degree the Rayleigh-Taylor instabilities would reduce the projected J-scaling law yields, and also how the radiation pulse shape would be effected. There have been suggestions for novel load configurations which employ snowplow or rotational [Ref.14] stabilization to mitigate load disruption. Multi-zone radiation-hydrodynamic 1-D (no instability) simulations of uniform fill implosions driven by a JUPITER prototype generator presented by J. Davis [Ref.6] show a factor of 2 reduction in the krypton yields compared to the optimal thin shell configuration. However, 2-D simulations without radiation suggest that a uniform fill can maintain stability starting with R_o as large as ~5 cm, while shells went unstable if $R_o \gtrsim 3$ cm. Further

investigations with 2-D $R - Z$ and $R - \theta$ radiation-hydrodynamic simulations could better test the stabilization and radiation potential of uniform fills, rotation, or even inverted density profiles. Continued investment in studies to *symmetrize and stabilize large radii implosions* is necessary to ensure the viability of PRS on JUPITER.

Acknowledgments

References

[1.] J. P. Apruzese and J. Davis, "K-Shell Yield Scaling Law for Conventional PRS Loads," *Naval Research Laboratory Memorandum Report*, No. 5406 (1984).

[2.] K.G. Whitney, J.W. Thornhill, J.P. Apruzese, and J. Davis, "Basic Considerations for Scaling Z-Pinch X-Ray Emission with Atomic Number," *J. Applied Physics*, 67, 1725 (1990).

[3.] J.W. Thornhill, K.G. Whitney, C. Deeney, and P.D. LePell, "Phenomenological Modeling of Turbulence in Z-Pinch Implosions," submitted to *Physics of Fluids B*, July, 1993.

[4.] K.G. Whitney, J.W. Thornhill, J.L. Giuliani Jr., J. Davis, L. Miles, G. Nolting, V. Kenyon, W. Speicer, R.B. Spielman, T.J. Nash, J.S. McGurn, L.E, Ruggles, C. Deeney, R.R. Prasad, and L. Warren, "Optimization of K-Shell Emission in Aluminum Z-Pinch Implosions: Theory versus Experiment," submitted to *Phys. Rev. E*, February (1994).

[5.] T. W. Hussey, N. F. Roderick, U. Shumlak, R. B. Spielman, and C. Deeney, "A Heuristic Model for the Non-Linear Rayleigh-Taylor Instability in Fast Z Pinches," Appendix to *Load Physics Report in JDOST Final Report*, (1994).

[6.] J. Davis, "Comments on Load Physics Issues," presentation at the *2'nd JDOST Workshop*, Naval Research Lab., September (1993).

[7.] J. Katzenstein, "Optimal Coupling of Imploding Loads to Pulse Generators," *J. Appl. Phys.*, 52, 676 (1981).

[8.] D. Mosher, *Naval Research Laboratory Memorandum Report*, No. 3687 (1978).

[9.] C. W. Mendel, Jr., M. E. Savage, D. M. Zager, W. W. Simpson, T. W. Grasser, and J. P. Quintenz, "Experiments on a Current-Toggled Plasma-Opening Switch," *J. Appl. Phys.*, 71, 3731 (1992).

[10.] D. D. Hinshelwood, "BERTHA – A Versatile Transmission Line and Circuit Code," *Naval Research Laboratory Memorandum Report*, No. 5185 (1983).

[11.] P. Corcoran, "Jupiter Adder Circuit Modeling," presentation at the *4'th JDOST Workshop*, Naval Research Lab., January (1994).

[12.] R.E. Reinovosky, D.L. Smith, W.L. Baker, J.H. Degnan, R.P. Henderson, R.J. Kohn, D.A. Kloc, and N.F. Roderick, "Inductive Store Pulse Compression System for Driving High Speed Plasma Implosions," *IEEE Trans. Plasma Sc.*, 10, 73 (1982).

[13.] I. Smith, personal communication.

[14.] A. Velikovich and J. Davis, Appendix to "Compression of a Rotating Z-Pinch Plasma," *Load Physics Report in JDOST Final Report*, (1994).